

Spatio-temporal Granger causality: a new framework

Qiang Luo^{1,2,3†}, Wenlian Lu^{3,4,5†}, Wei Cheng^{3,6,†}, Pedro A. Valdes-Sosa⁷, Xiaotong Wen⁸,
Mingzhou Ding⁸ and Jianfeng Feng^{1,3,4,5*}

¹Shanghai Center for Mathematical Sciences, Fudan University, Shanghai 200433, P.R. China

²Department of Management, School of Information Systems and Management, National University of
Defense Technology, Hunan 410073, P.R. China

³Centre for Computational Systems Biology, School of Mathematical Sciences, Fudan University,
Shanghai 200433, P.R. China

⁴Centre for Scientific Computing, University of Warwick, Coventry CV4 7AL, United Kingdom

⁵Fudan University-Jinling Hospital Computational Translational Medicine Centre, Fudan University,
Shanghai 200433, P.R. China

⁶Mathematical Department, Zhejiang Normal University, Jinhua 321004, PR China

⁷Cuban Neuroscience Center, Ave 25 #15202 esquina 158, Cubanacan, Playa, Cuba

⁸J. Crayton Pruitt Family Department of Biomedical Engineering, University of Florida, Gainesville,
Florida, US

[†] These authors contributed to this work equally.

*Correspondence should be addressed to Jianfeng Feng, Fudan University, Shanghai 200433, P.R. China. E-mail:
jianfeng64@gmail.com.

Abstract

It is the rule, not the exception, that physiological oscillations of various frequencies are present in fMRI signals. Here we proposed a novel theoretical framework - the spatio-temporal Granger causality - which allowed us to more reliably and precisely estimate Granger causality from experimental data sets possessing time-varying properties caused by the physiological oscillations. Within this framework, the Granger causality was redefined as a global index measuring directed information flow between time series with the time-varying properties. Both theoretical analyses and numerical examples demonstrated that the Granger causality was an increase function of the temporal resolution used in estimation, reflecting the general physics principle of coarse graining, which caused information loss by smoothing out very fine-scale details in time and space. This was confirmed by our results, which demonstrated that the Granger causality on the finer spatio-temporal scales considerably outperformed the traditional approach in terms of the improved consistency between two resting-state scans for the same subject. For practice, the proposed theoretical framework was implemented by combining several approaches, such as the optimal time window dividing and parameter estimation in the fine temporal and spatial scales to optimally estimate the Granger causality. Taken together, our approach provided a novel and robust framework to estimate the Granger causality from fMRI, EEG and related data.

Introduction

Granger causality, a standard statistical tool for detecting directional influence between system components, plays a key role in understanding system behaviour in many different areas, including finance (Chen et al., 2011), climate (Evan et al., 2011), genetics (Zhu et al., 2010) and neuroscience (Ge et al., 2012; Ge et al., 2009; Guo et al., 2008; Luo et al., 2011). The concept of Granger causality was originally proposed by Wiener in 1956 (Wiener, 1956), and introduced into data analysis by Granger in 1969 (Granger, 1969). This idea can be briefly described as follows: If the historical information of time series A significantly improves the prediction accuracy of the future of time series B in a multivariate autoregressive (MVAR) model, then the Granger causality from time series A to B is identified. In the classic Granger causality, time-invariant MVAR models are used to fit the observed time series experimental data.

However, a time-varying property is a common phenomenon in various systems. For example, the gene regulatory network in *Saccharomyces cerevisiae* was reported by Luscombe et al. (Luscombe et al., 2004) to evolve its topology, with respect to different stimuli or different life processes. A time-varying protein-protein interaction network for p53 was found by Tuncbag et al. (Tuncbag et al., 2009), who subsequently suggested the 4D view of the protein-protein interaction network with time as the 4th dimension. In the primary visual cortex of anaesthetized Macaque monkeys, ensembles of neurons have dynamically reorganized moment-to-moment effective connectivity (Ohiorhenuan et al., 2010). The importance of a slow oscillation, such as the theta rhythm, in a neuronal system is analysed in (Smerieri et al., 2010). It should be pointed out that even if the time series data were observed to be weakly stationary (i.e., stationary in the second moment), the configuration of the system could be time-varying. A typical example is $X_t = a \cos(\omega t + U_t) + \xi_t$, where t is time, a and ω are constants, $U_t \sim U[-\pi, \pi]$ is a uniform distribution, and ξ_t is noise. It is thus natural to consider time-varying systems and understand their impacts on the

estimation of the Granger causality.

Recently, analysing systems with time-varying structures has attracted increasing interest and many statistical methods have been proposed. An adaptive multivariate autoregressive model, via sliding short time windows, was proposed by (Ding et al., 2000) to deal with a non-stationary, event-related potential (ERP) time series. Inspecting directed interdependencies of Electroencephalography (EEG) data, a short time window approach to define the time-dependent Granger causality in (Hesse et al., 2003). The time-varying Granger causality has also been modelled by Markov-switching models in (Psaradakis et al., 2005; Warne, 2000). In these models, the time-varying Granger causality was modelled by a hidden discrete Markov process with finite state space. A wavelet-based time-varying Granger causality was suggested in (Sato et al., 2006) to establish the functional connectivity maps from fMRI data. Considering the time-series data as the independent and identically distributed observations, a method was proposed in (Ahmed and Xing, 2009) to infer the time-varying biological and social networks, but this method did not provide the directional information of the time-varying relationship between variables. The dual Kalman filter was used in (Havlicek et al., 2010; Sommerlade et al., 2012) to establish the time-varying Granger causality between non-stationary time series. These approaches extended the classic Granger causality analysis to the non-stationary case via adaptive multivariate autoregressive modelling under the assumption that the coefficients in the time-varying MVAR model can be modelled by random walk. As opposed to the literature that dealt with the time-varying properties in the MVAR model and defined Granger causality as a function with respect to time, we propose a robust *global* index measuring the directed information flow between time series, despite the time-varying properties. Granger causality is now a popular model for this purpose, but the classic Granger causality does not consider the time-varying properties in data. Moreover, it is a widely held misconception that the longer the time series we have, the more reliable the result we are able to obtain for Granger causality. The aims of this paper are twofold:

(1) We answer the question: What is the impact of the temporal scale in the MVAR models on the resulting directional influence of Granger causality? For Gaussian variables, the Granger causality is equivalent to the directed information transfer between variables. Hence the question becomes how the temporal scale in the MVAR model influences the estimation of the information flows between each variable within a system. In (Smith et al., 2011), the authors compared the performances of Granger causality analysis with different time lengths and found that the longer the time series was, the better the performance. However, in their simulations the underlying circuit stayed the same. In this paper, we will investigate the effects of the time-varying underlying circuits on the Granger causality analysis both mathematically and empirically.

(2) The second aim of this paper is to provide an efficient algorithm for estimating the global Granger causality index of between time series without any prior knowledge of the TV-MVAR model. It should be emphasised that there is a trade-off between the fineness of the change-point set and the accuracy of the estimation of the coefficients at each time window. Time windows that are too short might prevent a reliable estimation of the parameters; time windows that are too long might increase the probability of the incorrect inference of Granger causality. Based on Bayesian information criterion (BIC) and a change-point searching algorithm, we proposed a method to search for the optimal size of change-point set and the optimal change-points, in order to achieve the optimal balance between the fineness of the Granger causality and the accuracy of the model estimation. The theoretical results and the algorithms were verified by estimating the average and cumulative Granger causalities on simulated and experimental data, both of which confirmed that a finer change-point set gives a larger overall causality measurement.

To achieve the above goals, the effect of time-varying causal structure on the Granger causality analysis was investigated mathematically in this paper with the following

notations. Consider two time series x and y over a time window $[0, T]$. A *change-point set* $S_1 = \{0 = t_0 < t_1 < \dots < t_m = T\}$ defines the time-varying property of the MVAR model as follows: at each time window $[t_{k-1}, t_k)$, the MVAR model is static, i.e., the interacting coefficients between variables are constants, but in different time windows these may differ. Thus, it becomes a time-varying MVAR (TV-MVAR) model. There are two alternatives for estimating the Granger causality from y to x in the TV-MVAR model with respect to the change-point set S_1 . One is to estimate the local Granger causality at each time window $[t_{k-1}, t_k)$ and then average them, termed the *average Granger causality*, $F_{y \rightarrow x}^{(a, S_1)}$. The other is to average the variances of the residual errors locally at each small time window, so that the *cumulative Granger causality*, $F_{y \rightarrow x}^{(c, S_1)}$ can be established by comparing the estimated variances of residual errors of x by considering whether y can predict the future of x or not. The TV-MVAR model depends on the change-point set that divide the whole duration into finer time windows, as shown in Figure 1. Hence, we need to address the relationship between the causality definition and the fineness of the change-point set in the TV-MVAR model.

We proved that both the cumulative Granger causality and the average Granger causality are, in general, monotonically increasing functions with respect to the fineness of the change-point set (see Figure 1 for summary and Appendices A, B, and C for the proofs of the theories). That is, the finer the TV-MVAR model is, the larger the change-point set is, and the larger the (average and cumulative) Granger causalities that can be estimated. Particularly, as shown in Theorems B1 and B4, under some assumptions, in the coarser MVAR model, the estimation of the coefficients is the (weighted) average among those of the finer model. Hence, if the “true” time-varying coefficients are nonzero but fluctuate around zero, then the “averaging” estimation may reduce the estimated Granger causality to zero and give

an incorrect inference of Granger causality.

Empirically, we demonstrated the robustness of the proposed spatio-temporal Granger causality analysis by computing Pearson's correlation coefficients between the Granger causality patterns by using two scan sessions on the same subject from the enhanced Nathan Kline Institute-Rockland Sample (see Materials and Methods). By considering the spatio-temporal details of the fMRI data for the TV-MVAR model, the Granger causality had much better consistency across two scan sessions for the *same* subject. In particular, the correlation coefficient greatly increased from 0.3588 using the classic Granger causality with static MVAR model and region-wise estimation, to 0.6059 through our approach, including optimal TV-MVAR model and voxel-wise estimation.

The theoretical results have also been confirmed on two experimental fMRI data sets, including a resting-state data set and a task-associated data set. On the resting-state fMRI dataset, the classic Granger causality analysis failed to identify any significant causal connectivity to the precuneus. In comparison, within a finer-scale for the TV-MVAR model, our Granger causality approaches indicated that the precuneus served as a hub for information transfer in the brain. Information flows between the precuneus and the visual regions were revealed, consistent with the experimental setting that the data was collected with subjects' eyes open. On the task-associated fMRI dataset, the average Granger causality estimated for the attention blocks were found to be significantly larger than those estimated by the classic Granger causality based on static MVAR model for the whole time series for all 12 subjects in the experiment.

Materials and Methods

Generation of Time Series with Time-varying Causal Structure

1) Generation of Time Series with Continuous Time-varying Causal Structure

Consider two time series and the effective interdependencies between them were

described by the TV-MVAR model with constant noise level. The time-series were generated by the following toy model

$$\begin{pmatrix} x^{t+1} \\ y^{t+1} \end{pmatrix} = \begin{pmatrix} A_{11}(t) & A_{12}(t) \\ A_{21}(t) & A_{22}(t) \end{pmatrix} \begin{pmatrix} x^t \\ y^t \end{pmatrix} + \begin{pmatrix} n_{xy}^t \\ n_{yx}^t \end{pmatrix}, \quad (1)$$

where

$$A_{11}(t) = 0.1, A_{12}(t) = 0.5 \left(\frac{t}{600} - 1 \right) \cdot u_1,$$

$$A_{21}(t) = 0.5 \left(1 - \frac{t}{400} \right) \cdot u_2, A_{22}(t) = 0.1\sqrt{2}.$$

We generated 100 times of this toy model by randomly setting the parameters u_1 and u_2 according to the uniform distribution on the interval of $[0,1]$. For each model, the time series observations were generated for 1200 time steps. The parameters A_{12} and A_{21} corresponded to the causal influences at the directions $Y \rightarrow X$ and $X \rightarrow Y$, respectively. A significant nonzero causal coefficient means the causal influence at the corresponding direction. In this simulation, we specified the causal coefficient change from positive to negative.

2) Generation of Time Series with Stepwise Time-varying Causal Structure

Consider a TV-MVAR model of two components with only one directional causal influence, $X \rightarrow Y$, namely setting the corresponding coefficient A_{21} to have nonzero values. The model came from Eq. (1) with the step-wise coefficients as follows

$$A_{11}(t) = 0.1, A_{22}(t) = 0.1\sqrt{2},$$

$$A_{12}(t) = 0, A_{21}(t) = \begin{cases} 0.5u_1, & 0 < t \leq t_1 \\ 0, & t_1 < t \leq t_2 \\ -0.5u_1, & t_2 < t \leq t_3 \\ 0, & t_3 < t \leq T \end{cases} \quad (2)$$

where $t_1 = 215$, $t_2 = 415$ and $t_3 = 715$. We generated two time series with 1200 time points and repeated this generation 100 times by randomly setting the parameter u_1

from a uniform distribution on the interval of [0.5,1.5]. In this simulation, the causal coefficient A_{12} for the direction $Y \rightarrow X$ was set zero, so no causal influence from Y to X and the causal coefficient A_{21} varied across different time windows.

3) Generation of BOLD Signal with Time-varying Effective Connection

Here we simulated the fMRI time series of two brain regions, X and Y , for 400 seconds. By introducing the time-varying causal structure, the simulation scheme for fMRI data in (Schippers et al., 2011) was adopted. First, the neuronal interaction (the local field potential, LFP) was simulated by using a bi-dimensional first-order TV-MVAR model with the time step of 10 milliseconds:

$$\begin{pmatrix} x^{t+1} \\ y^{t+1} \end{pmatrix} = A \begin{pmatrix} x^t \\ y^t \end{pmatrix} + \begin{pmatrix} n_{xy}^t \\ n_{yx}^t \end{pmatrix}, \quad (3)$$

where

$$A_{11} = 0.9, A_{22} = 0.9,$$

$$A_{12} = 0, A_{21} = \begin{cases} 0.5, & 0 < t \leq 18000 \\ -0.5, & 18000 < t \leq 40000 \end{cases}$$

The model embodied an influence from X to Y of a predetermined time-varying strength A_{21} and no influence from Y to X .

Second, both signals were convolved with the default hemodynamic response models from SPM5 toolbox and Gaussian noises were added as physiological noise in the BOLD response. The HRF was specified by seven model parameters: delay of response relative to onset (in seconds), delay of undershoot relative to onset (in seconds), dispersion of response, dispersion of undershoot, ratio of response to undershoot, onset (in seconds), and length of kernel. To investigate the effect of hemodynamic response variability on Granger causality analysis, we systematically varied the delay of response ranging from 0 second to 5 seconds. To mimic the neuronal delay between the cause-region to the effect-region, time series Y was shifted by 50 milliseconds against X before the convolution of HRF (Deshpande et al., 2010; Schippers et al., 2011; Smith et al., 2012).

Third, the BOLD signals were generated by down-sampling the convolved time series by 2Hz as a high sampling rate and 1Hz as a low sampling rate (resembling an acquisition rate (TR) of an MR-scanner) and Gaussian noise was again added as acquisition noise. After each step the signals were normalized to zero means and unit variances. The total amount of noise added was 20%.

Experimental fMRI Data Sets

1) Multiband Imaging Test-Retest Pilot Data Set

This set of fMRI data was from the enhanced Nathan Kline Institute-Rockland Sample. The whole dataset consisted of resting-state fMRI recordings in two sessions for 17 subjects (healthy, ages 19-57, and 4 females).

The fMRI data were collected using 3 Tesla and 40 slices were acquired for 900 volumes. Multiband echo planar Imaging approaches enable the acquisition of fMRI data with unprecedented sampling rates ($TR=0.645s$) for full-brain coverage through the acquisition of multiple slices simultaneously at the same time. For more detailed information about this data set, please see the website http://fcon_1000.projects.nitrc.org/indi/pro/eNKI_RS_TRT/FrontPage.html.

Data pre-processing was performed by the DPARSF software (Yan and Zang, 2010). The first 50 volumes were discarded to allow for scanner stabilisation. Since multiple slices were excited simultaneously, simple slice time correction might not work well. Given the short effective TR it is probably less important, so it is omitted in our data pre-processing. After the realignment for head-motion correction, the standard Montreal Neurological Institute (MNI) template provided by SPM2 was used for spatial normalization with a re-sampling voxel size of $3 \times 3 \times 3 \text{ mm}^3$. After smoothing (FWHM=8mm), the imaging data were temporally filtered (band pass, 0.01~0.08Hz) to remove the effects of very low-frequency drift and high-frequency noises (e.g., respiratory and cardiac rhythms). An automated anatomical labelling (AAL) atlas (Tzourio-Mazoyer et al., 2002) was used to parcellate the brain into 90 regions of interest (ROIs). To verify the principle of voxel-level Granger causality, the brain was also divided into 1024 ROIs with around 45 voxels each according to a high-resolution brain atlas provided by (Zalesky et al., 2010).

2) Resting-State fMRI Data Set

The resting-state fMRI data set was a subset of a large database, called “1000

Functional Connectomes Project” (Biswal et al., 2010), which was freely accessible at the website: www.nitrc.org/projects/fcon_1000/. Here, the dataset provided by Buckner’s group at Cambridge, USA, was used for the present study. This data set consists of 198 healthy subjects (75 males, 123 females and ages 18-30). The fMRI data (TR = 3s) were collected using 3 Tesla and 47 slices were acquired for 119 volumes. More detailed information about this data set can be found on the website mentioned above.

The first 5 volumes were discarded to allow for scanner stabilization. The DPARSF(Yan and Zang, 2010) based on SPM8 was used for pre-processing the fMRI data, including slice-timing correction, motion correction, co-registration, grey/white matter segmentation, and spatially normalization to Montreal Neurological Institute (MNI) space and resampled to $3 \times 3 \times 3 \text{ mm}^3$. The waveform of each voxel was detrended and passed through a band-pass filter from 0.01 Hz to 0.08 Hz. The data were smoothed spatially (FWHM=8 mm). In results, the time series data with 114 time points of 90 brain regions (AAL-atlas) for 198 subjects were achieved.

3) fMRI Dataset for Attention-Task

The dataset of fMRI time series for an attention-task experiment was provided by Ding Group at the University of Florida, USA (Wen et al., 2012), which consisted of 12 subjects who successfully completed the task (8 females, 4 males, ages 20-28). This experiment adopted a mixed blocked/event-related design. There were 12 attention blocks and 12 passive-view blocks, together with some fixation intervals. In each attention block, the subject performed a trial-by-trial cued visual spatial attention task. The fMRI data were collected using 3 Tesla and 33 slices were acquired for 180 volumes for each of the six runs with TR 2s. The data set was pre-processed by slice timing, motion correction, co-registration to individual anatomical image, normalization to the Montreal Neurological Institute (MNI) template, and resampled to $3 \times 3 \times 3 \text{ mm}^3$, using DPARSF. The hemodynamic response function (HRF) was convolved by the blocked rectangular function corresponding to a given experimental

condition during the GLM analysis. For more detailed information about this dataset, please see (Wen et al., 2012).

For each attention block, there were 30 data points, lasting for 60 seconds. The task average response was removed from each attention block by subtracting the mean of the time series data across 12 attention blocks. The first 5 data points (10 seconds) were discarded to eliminate transient effects. The temporal mean was removed for each attention block to meet the zero mean requirement of the Granger causality analysis. Therefore, we had 300 data points for the 12 attention blocks. Here, the causality between the right intra-parietal sulcus (rIPS) and the right temporal-parietal junction (rTPJ) was studied. There were time series of 19 voxels and 17 voxels for the rIPS and rTPJ respectively (Wen et al., 2012).

Granger Causality in TV-MVAR

For two time series x^t and y^t with $t = 1, 2, \dots, T$. Define a change-point set as an increasing integer series: $1 = t_0 < t_1 < \dots < t_{m-1} < t_m = T + 1$, denoted by S_1 . Consider the following piece-wise constant linear system to describe the directional influence from y^t to x^t as follows:

$$x^{t+1} = \bar{a}_1^{S_1}(k)x^t + \bar{b}_1^{S_1}(k)y^t + n(t), t_{k-1} \leq t < t_k, k = 1, \dots, m \quad (4)$$

where $\bar{a}_1^{S_1}(k)$ and $\bar{b}_1^{S_1}(k)$ are estimated time-varying coefficients, due to S_1 . Also, if ignoring the directed causality from y^t to x^t , then Eq. (4) becomes

$$x^{t+1} = \tilde{a}_1^{S_1}(k)x^t + \tilde{n}(t), t_{k-1} \leq t < t_k, k = 1, \dots, m \quad (5)$$

where $\tilde{a}_1^{S_1}(k)$ is the estimated time-varying coefficient in this model. At the k^{th} time window, the Granger causality can be defined locally as

$$F_{y \rightarrow x}^{(k, S_1)} = \log \left[\frac{\sum_{t=t_{k-1}}^{t_k-1} \text{var}(\tilde{n}(t))}{\sum_{t=t_{k-1}}^{t_k-1} \text{var}(n(t))} \right].$$

The average Granger causality with respect to S_1 can be estimated by the average of Granger causalities at the time windows and weighted by the corresponding window lengths:

$$F_{y \rightarrow x}^{(a, S_1)} = \frac{1}{T} \sum_{k=1}^m F_{y \rightarrow x}^{(k, S_1)} (t_k - t_{k-1}). \quad (6)$$

If the length of each time window is uniform, it becomes

$$F_{y \rightarrow x}^{(a, S_1)} = \frac{1}{m} \sum_{k=1}^m F_{y \rightarrow x}^{(k, S_1)}.$$

The alternative way to compute the Granger causality is cumulating the residual square errors across all time windows. This is called the cumulative Granger causality with respect to S_1 and can be estimated by:

$$F_{Y \rightarrow X}^{(c, S_1)} = \log \left[\frac{\sum_{t=1}^T \text{var}(\tilde{n}(t))}{\sum_{t=1}^T \text{var}(n(t))} \right] = \log \left[\frac{\sum_{k=1}^m \sum_{t=t_{k-1}}^{t_k-1} \text{var}(\tilde{n}(t))}{\sum_{k=1}^m \sum_{t=t_{k-1}}^{t_k-1} \text{var}(n(t))} \right]. \quad (7)$$

In particular, if the random variable y^t is stochastically orthogonal to x^t at each time, i.e., $E[(x^t - Ex^t)(y^t - Ey^t)] = 0$ for all t , the cumulative Granger causality can be estimated as:

$$F_{Y \rightarrow X}^{(c, S_1)} = \log \left[\frac{\sum_{k=1}^m \sum_{t=t_{k-1}}^{t_k-1} [a_1(t) - \tilde{a}_1^{S_1}(k)]^2 \text{var}(x^t) + \sum_{k=1}^m \sum_{t=t_{k-1}}^{t_k-1} [b_1(t)]^2 \text{var}(y^t) + \sum_{k=1}^m \sum_{t=t_{k-1}}^{t_k-1} \text{var}(n(t))}{\sum_{k=1}^m \sum_{t=t_{k-1}}^{t_k-1} [a_1(t) - \bar{a}_1^{S_1}(k)]^2 \text{var}(x^t) + \sum_{k=1}^m \sum_{t=t_{k-1}}^{t_k-1} [b_1(t) - \bar{b}_1^{S_1}(k)]^2 \text{var}(y^t) + \sum_{k=1}^m \sum_{t=t_{k-1}}^{t_k-1} \text{var}(n(t))} \right].$$

For the details of the derivative of the expressions for the Granger causalities, please see Appendix A. Here, only the first-order regression model with one-dimensional variables is considered, but the approach and results work for general high-order and high dimensional TV-MVAR model that will appear in our near future paper.

Since in each time window $F_{y \rightarrow x}^{(k, S_1)}$ obeys F -distribution after proper scaling, the average Granger causality defined above can be considered in the null hypothesis as the summation of m independent F -distributed random variables whose degree-of-freedoms can be given according to the number of free parameters and the

length of each time window, particularly, 1 and $t_k - t_{k-1} - 3$. Therefore, the p -value for the significance of the average Granger causality can be calculated. Similarly, the cumulative Granger causality defined above also obeys the F -distribution with the degree-of-freedoms, m and $T-2m-1$.

Optimal Time Window Dividing

In practice, the *true* time-varying structure of the data is unknown. In particular, we do not know how many change-points are and how long of each time window is. Therefore, an algorithm for time window division is necessary. Equivalently, we are to search the optimal change-point set. The optimal time-window dividing means a trade-off between the satisfactory accuracy of the model parameter estimation and the lossless causal information established by the model. Mathematically, considering the following step-wise TV-MVAR model

$$X(t+1) = \sum_{k=1}^m a_1^k X(t) I_{[t_{k-1}, t_k)} + n(t), \quad (8)$$

where $I_{[t_{k-1}, t_k)}$ is the characteristic function of the time window $[t_{k-1}, t_k)$, $n(t)$ is the Gaussian white noise term, a_1^k represents the (constant) coefficient in the k^{th} interval, and

$$S(m) = \{t_1, \dots, t_{m-1} \mid 1 = t_0 < t_1 < \dots < t_{m-1} < t_m = T + 1\}$$

is the change-point set. Given the change-points, the model can be fitted in each time window as \hat{a}_1^k , and the variance of the residual errors can also be estimated for each time window, denoted by $\hat{\Sigma}_k$. Therefore, the accuracy of the model can be defined by the weighted average of the variances of the residuals in each time window as follows:

$$err(S(m)) = \frac{1}{m} \sum_{k=1}^m (t_k - t_{k-1}) \det(\hat{\Sigma}_k). \quad (9)$$

On the other hand, the information captured by this model can be measured by the average Granger causality in all directions defined in the previous section, noted by

$$agc(S(m)) = \frac{1}{2m} \sum_{k=1}^m (F_{y \rightarrow x}^{(k, S(m))} + F_{x \rightarrow y}^{(k, S(m))}). \quad (10)$$

To minimize the prediction error and maximize the detected causality information, the optimal window dividing can be derived by optimising the following cost function with a trade-off parameter λ

$$S_{opt}(m, \lambda) = \arg \min_{S(m)} (err(S(m)) + \lambda/agc(S(m))). \quad (11)$$

Given a trade-off parameter λ_0 and a lower bound l_0 of the lengths of the divided time windows, the optimal change-points $S_{opt}(m, \lambda_0)$ can be established by solving the following constrained optimization problem

$$\min_{S(m)} (err(S(m)) + \lambda_0/agc(S(m))) \quad (12)$$

$$\text{s.t. } t_k - t_{k-1} \geq l_0 \text{ for all } k = 1, 2, \dots, m.$$

The constrained condition is required towards a reliable estimation of the model coefficients in Eq. (8) at each divided time window. This constrained optimization problem can be solved by the optimization functions provided in Matlab. In this paper, we used the function *fmincon* for nonlinear constrained optimization problem.

To determine the parameter, we search the optimal change-point set $S_{opt}(m, \lambda)$ for different $\lambda \in [\lambda_1, \lambda_2]$ and calculate the Bayesian information criterion (BIC) for this change-point set as follows:

$$BIC(m, \lambda) = -2 \sum_{k=1}^m LLF_k + 2^2 m \log(T+1), \quad (13)$$

where LLF_k stands for the log likelihood function established for the k^{th} window. Searching for the optimal change-point set with a series of given number of time windows, $m \in [0, 1, 2, \dots, m_0]$, and trade-off parameter, $\lambda \in [\lambda_1, \lambda_2]$, is the first step; the second step is to compare the BIC values established by different change-point sets generated from the first step, and then the one with the smallest BIC is selected to define the optimal time window. Therefore, with fixed upper bound of the number of

time windows, denoted by m_0 , the algorithm for optimal time window dividing is described as follows:

Algorithm for optimal time window dividing

For $\lambda =$ from λ_1 to λ_2

For $m =$ from 1 to m_0

Establish $S_{opt}(m, \lambda)$ by solving the constrained optimization problem (12)

End

Calculate BIC for each $S_{opt}(m, \lambda)$ by (13)

End

Find the optimal $S_{opt}(m_{opt}, \lambda_{opt})$ with the smallest BIC

Spatio-temporal Granger Causality

Furthermore, both spatial and temporal fineness are taken into the MVAR model. The idea of spatial finer-scale for Granger causality estimation was similar to that of the time-varying Granger causality we mentioned above. Consider a dataset of fMRI BOLD signals from m voxels in ROI A and n voxels in ROI B . For each pair of voxels in these two ROIs respectively, the Granger causality between the voxel pair is calculated for each subject, denoted by F_{ij} from the i th voxel in ROI A to the j th voxel in ROI B ; and then the *global* Granger causality from ROI A to ROI B , namely *voxel-level Granger causality*, is defined as:

$$F_{A \rightarrow B} = \frac{1}{mn} \sum_{i \in ROI_A} \sum_{j \in ROI_B} F_{ij}.$$

Furthermore, the temporal and the spatial fine-scale are combined together to give optimal estimation of Granger causality by looking into the temporal details for each pair of voxels, called the *spatio-temporal Granger causality* (spGC):

$$F_{A \rightarrow B}^{(e,S)} = \frac{1}{mn} \sum_{i \in ROI_A} \sum_{j \in ROI_B} F_{ij}^{(e,S)},$$

with $e = a$ or c for average and cumulative (time-varying) Granger causality respectively. In comparison, the classic Granger causality usually estimates the causality between two ROIs by averaging the time series data among all voxels for each ROI with a static MVAR model.

Results

Monotonicity of Granger Causality with Respect to Change-point Set

To demonstrate the monotonicity of the proposed Granger causality measurements, the proposed algorithms were applied to the simulation data set with continuous time-varying causal structure. We used three different time window lengths, 50, 200, and 400, and the corresponding change-point sets for these time windows were denoted by $S_i, i = 1, 2, 3$, respectively. Theorems B1 and B4 in Appendix B show that

$F_{Y \rightarrow X}^{a,S_1} \geq F_{Y \rightarrow X}^{a,S_2} \geq F_{Y \rightarrow X}^{a,S_3}$ and $F_{Y \rightarrow X}^{c,S_1} \geq F_{Y \rightarrow X}^{c,S_2} \geq F_{Y \rightarrow X}^{c,S_3}$ hold if the parameters are precisely estimated since $S_1 \supset S_2 \supset S_3$. To demonstrate that, the 95% confidence intervals of

$D_1^a = F_{Y \rightarrow X}^{a,S_1} - F_{Y \rightarrow X}^{a,S_2}$, $D_2^a = F_{Y \rightarrow X}^{a,S_2} - F_{Y \rightarrow X}^{a,S_3}$ and $D_3^a = F_{Y \rightarrow X}^{a,S_1} - F_{Y \rightarrow X}^{a,S_3}$ were established for

the causality results in 100 runs of the simulation toy model. Similarly, $D_i^c, i = 1, 2, 3$ were defined and their confidence intervals were established, too. From Table 1, we can see that the estimated Granger causality for the same pair of time series decreases with respect to the length of time windows. That's to say, the more change-points are used in the TV-MVAR model, i.e., the finer the model is, the larger the Granger causality can be estimated.

To show the accuracies of the model estimation, we compared the differences between the variances of the model residual errors given by different algorithms, including the static MVAR model by the whole time series, denoted by $Err_{[1,1200]}$, and the average variances of the model residual errors for the TV-MVAR model over time windows,

\overline{Err}_{S_i} , as $D_i = Err_{[1,1200]} - \overline{Err}_{S_i}$ for $i = 1, 2, 3$. As shown in Figure 2A, the TV-MVAR models with different time-window lengths all have smaller variances than the static MVAR model fitted on the whole time series for all 100 toy models, i.e., the $D_i > 0$ holds for 100 runs of the toy model. Among the models with different time window sets, the one with the smallest length of the time window, i.e., which had S_1 as the change-point set, gave the most accuracy estimation of the simulated time series.

Significance of Granger Causality

To compare the significance of the results detected by our time-varying Granger causality approach with those by the classic Granger causality, we applied these algorithms on the simulation data set with stepwise causal structure. If the p -value was lower than a threshold, a significant directional influence was detected. In this simulation setup, the causal influence existed from X to Y , but did not from Y to X . The usual definitions of the truth positive (TP), false positive (FP), truth negative (TN) and false negative (FN) were used, the maximum number of the time windows is set as $m_0 = 5$, and the trade-off parameter ranged from $\lambda_1 = 0.02$ to $\lambda_2 = 1$ with the step size 0.02. Five types of Granger causalities, the classic Granger causality (classic GC), the average Granger causality (average GC), the cumulative Granger causality (cumulative GC), the average Granger causality with optimally divided time windows (Opt average GC), the cumulative Granger causality with optimally divided time windows (Opt cumulative GC) were calculated based on the simulation data with significance test.

As shown in Table 2, the classic GC failed to identify any causal influence between these two time series. The cumulative GC and average GC gave better results in terms of higher TP and TN rates than the classic GC. Compared to other algorithms, the average GC and the cumulative GC with optimally time window dividing gave the best performance in terms of the TP and the TN rates among all. In particular, as

shown in Theorems B1 and B4, under our assumption, in the coarser MVAR model, the estimation of the coefficients is the (weighted) average of those of the finer model. As an intuitive interpretation, if the “true” time-varying coefficients are nonzero but have their signs fluctuating, for example, it equals to 1 at the first time interval and -1 at the last time interval with equal length, and then the “averaging” estimation becomes zero due to the neutralisation, even if the coefficient parameters are precisely estimated. Thus, in the static MVAR model, we will incorrectly infer that there is no Granger causality. The similar argument holds for the comparison of finer and coarser MVAR models. Therefore, the coarseness of the TV-MVAR model might increase the probability of incorrect inference of the Granger causality.

To demonstrate the performance of the optimal GC estimations by using time windows with equal lengths, we compared the accuracies of the results given by the optimal GCs with different lengths of time windows. We found that the better performances were achieved if their time window dividing was similar to the *real* structure of the simulation data. Since the real change-points of this simulation were 215, 415 and 715, both the algorithms presented better results when the lengths of time windows were 100 or 300. In comparison, the performances became worse when the lengths of time windows were longer or shorter.

After testing whether the larger magnitude of Granger causality estimated by the optimal GCs increases the false positive (FP) rate, we found that the FP rates of both the cumulative GC and the average GC with different window lengths were zeros if the threshold of significance was 10^{-12} (for the F statistics). Therefore, the FP rates of these two algorithms did not increase with respect to the GC values, as the lengths of time windows went shorter. Since the degree-of-freedoms of the F statistics depended on the number of change-points, the GC value became larger with shorter time windows. However, since the corresponding F distribution also changed with the number of change-points, the FP rates might not increase.

To assess the rationality of the BIC-based optimal time window dividing algorithm, the BIC values were also reported and compared among the simulations. As shown in Table 2, good BIC values were achieved if the change-point set for the average GC and the cumulative GC was similar to the true structure of the simulated data. This suggested that the BIC values can work for choosing change-points to achieve the best performance. We chose the change-point set optimally instead of using the time windows with equal lengths. Table 2 also showed that compared to the algorithms with equal time window dividing, the algorithms with optimally change-point searching gave better TP rates, but the slightly worse FP rates, namely 3% for the Opt cumulative GC and 2% for the Opt average GC on the simulation data. Figure 2B shows that the real change-points for 100 simulations by the proposed BIC-based optimal algorithm were successfully identified for most simulations.

To compare the computational complexities among different algorithms, we reported the running time of the algorithms on the simulated data set. As listed in Table 3, the more time windows we used, the longer the time was required for running the algorithm, because the method for optimally dividing the time windows was very time-consuming. In practice, since the underlying time-varying structure of the data is unknown, we can either run the optimally time-window dividing algorithm, or try different time window lengths and select one optimal time window length, by comparing their BIC's.

Effect of Regional Variation in HRF on Granger Causality Analysis

The effects of HRF delay of response on the Granger causality analysis were simulated by setting the delay of response relative to onset of the HRF for brain region X as this parameter for brain region Y plus a delay ranging from 0 milliseconds to 100 milliseconds. Therefore, the underlying causal influence existed from X to Y , but the HRF of the cause-region X was slower than the effect-region Y . We referred to this delay as *opposite HRF delay*. The longer this delay is the more difficult for the Granger causality analysis to detect the causal influence correctly. Setting the

threshold of p -value for significant causality as 10^{-6} , Figure 2C plots the TP rates and the FP rates of different algorithms varied as the opposite HRF delay varying from 0 second to 3 seconds. The Opt average GC and the Opt cumulative GC performed similarly in the simulation, so the results were shown for Opt average GC only. We can see that the optimal Granger causality performs well as long as the opposite HRF delays less than 100 milliseconds. When the opposite HRF delay was greater than 100 milliseconds, the FP rate increased and the TP rate dropped rapidly. The TP rate increased again when the opposite HRF delay exceeded 0.4 second, since the opposite HRF delay was generated by changing the shape of the HRF (Deshpande et al., 2010). We have also carried out our simulations by changing the onset time of the HRF instead of changing its shape, and similar results were obtained (data not shown).

To test if the opposite delay in HRF can be corrected for the optimal GC algorithms, we realigned the simulated BOLD signal according to the HRF delay between two regions by assuming that the regional HRF, especially the relative HRF delay between two regions, can be accurately estimated. For example, if the HRF of region Y was estimated to be 3 seconds faster than that of region X , we realigned the time series of the region X against that of the region Y by discarding the first 3 data points of the time series of region X and the last 3 data points of the time series of the region Y , when the sampling rate was 1Hz. The regional HRF delay was simulated by setting different parameters of the response relative to onset in the canonical HRF in SPM with default settings, and the opposite HRF delay varied from 2 to 5 seconds. Figure 3A presents the results given by the GC algorithm with BOLD signal realignment, when the sampling rate of the BOLD signal was 1Hz. Setting the threshold of 10^{-9} for the p -value, the classical GC failed to detect any causality in this case, but the proposed GC algorithms achieved much better TP and FP rates. However, the BOLD realignment worked for those integer HRF delays matching the sampling rate, but not for those delays which are not the integer times of the sampling period, here it is 2.5, 3.5, and 4.5 seconds. Therefore, we tried to increase the sampling rate to 2Hz, and simulated the BOLD signal again. In Figure 3B, without the BOLD realignment, the

proposed GC algorithms failed to reliably estimate the causality as both the TP and FP are high. The BOLD realignment improved the performances of the proposed GC algorithms with a 100% TP rate and less than 20% FP rate as shown in Figure 3C. We can barely see the results for the classic GC in Figure 3, since the classic GC failed to detect any significant causal causality in all cases.

As demonstrated above, the proposed optimal GC algorithms may detect the right direction of the causal influence between two regions, the reversed direction, or the bi-direction to be significant. What if no causal influence between two regions? To test whether the down sampling and HRF convolution introduce false causal connections between pairs of regions without any causal influence in neuronal activities, the proposed algorithm were applied to another simulation data by setting the causal coefficient A_{21} in model (3) to be zero, the neuronal delay 50 milliseconds, and the opposite HRF delay 3 seconds. Setting the threshold of p -value for significant causality as 10^{-6} , the false positive rates for Opt average GC and Opt cumulative GC were 0.24% and 0.12%, respectively.

Performance Comparison on Simulated fMRI Dataset

First, the classic Granger causality (classic GC), the optimal GC approaches (Opt average GC and Opt cumulative GC) and the dual Kalman filter cumulative GC (Dkf cumulative GC), with its definition in Appendix D, were applied to the simulated fMRI dataset described above for performance comparison. All results were obtained by repeating the simulation for 100 times. Neither the neuronal delay nor the negative HRF delay was included in this simulation as none of the lag-based methods working well in that case (Smith et al., 2011), but this performance comparison would be informative when the lag-based method is applicable (Wen et al., 2012). If the coefficient matrix A was time-invariant, all approaches can detect the causality correctly, as one expected. When the interaction coefficients were time-varying, in particular, with positive and negative values alternatively in different time intervals, as defined in Eq. (3), the optimal GC approaches were much more powerful than both

the classic GC and the dual Kalman filter cumulative GC. To get more global view of the results, the threshold of the p -values was varied from 0.05 to 0.001. We calculated the TP rates and the FP rates of these three approaches: Opt average GC, Opt cumulative GC and Dkf cumulative GC, accordingly by repeating the simulation 100 times. As shown in Figure 2D, the proposed optimal GC approaches outperformed the dual Kalman filter cumulative GC.

Increased Test-retest Reliability Obtained on Multiband Resting-State Dataset

Here, the reliability of Granger causality can be measured by the correlation between the results inferred for two series of scans on the same subjects. The Granger causality was estimated between all directional pairs of the brain regions, and then the Pearson's correlation coefficients were calculated between these causality measurements for the two series scans respectively. For each scan in the multiband test-retest pilot dataset, the Granger causality for each direction was averaged over 17 subjects to give the group Granger causality. The correlations of the group Granger causality between two series of scans demonstrate the reliability of the Granger causality. If the correlations were larger, then reliability might be higher. As shown in Figure 4, the correlations in the group Granger causality between two series of scanning increased monotonically with respect to the number of change-points. A significant correlation ($r = 0.4751$, $p < 0.001$) in the group Granger causality between two series of scanning were observed when the Granger causality was calculated by employing 19 time windows, while the correlation was around 0.3105 in the classical case.

To further demonstrate the effect of the spatial fine-scale details on the Granger causal inference, in 100 randomly selected regions from 1024 ROIs, we compared the correlations established by the voxel-level Granger causality with those by the classic Granger causality, by averaging the time series in the same ROI. The correlation increased from 0.3588 to 0.5125 by calculating the voxel-level spatial Granger causality instead of the classic Granger causality. Furthermore, the combined effects

of the temporal and spatial fine-scale details were demonstrated on the test-retest reliability of the Granger causality for 100 regions randomly selected from 1024 ROIs. In Figure 5, the correlation ($r = 0.6059$, $p < 0.001$) between two scans is significantly improved to 0.6059 by calculating the spatial and temporal Granger causality.

Validating Results on the Resting-State fMRI Dataset

1) Monotonicity and significance of Granger causality

In this example, the Granger causality was estimated by using the time windows with different lengths. In each time series, the first 80 time points were divided into two sets of time windows, including 8 time windows with 10 time points per window, i.e., a change-point set $S_1 = \{1, 10, 20, 40, 50, 60, 70, 80\}$ and 2 time windows with 40 time points per window, i.e., a change-point set $S_2 = \{1, 40, 80\}$. The cumulative and average Granger causalities with S_1 and S_2 were estimated for all directions between all pairs of brain regions for each subject. The 95% confidence intervals of the differences $D_{j \rightarrow i}^a = F_{j \rightarrow i}^{a, S_1} - F_{j \rightarrow i}^{a, S_2}$ and $D_{j \rightarrow i}^c = F_{j \rightarrow i}^{c, S_1} - F_{j \rightarrow i}^{c, S_2}$ were established for all possible directions $\{i \rightarrow j \mid i, j = 1, 2, \dots, 90 \text{ and } i \neq j\}$. For all directions, the lower bounds of these differences were still larger than 0, which was exactly consistent with our theoretical results, as shown in Figure 6B.

The results of the average and cumulative Granger causalities were well correlated, as shown in Figure 6A. Actually, if the data are generated by the TV-MVAR model that exactly static in each time window, the cumulative Granger causality is larger than the average Granger causality (See Theorem C1 in Appendix C). Under the null hypothesis of non-causality, both Granger causalities approach zeros as the size of data becoming sufficiently large. Moreover, the average Granger causality converges to zero quicker than the cumulative Granger causality (Theorem C2 in Appendix C), i.e., the p -value of significance of the average Granger causality may be smaller, as also shown by the simulation results in the previous section (Table 2) that the average

Granger causality performs better than the cumulative Granger causality in terms of detecting non-causality. Therefore, in the following, the average Granger causality was calculated.

As discussed in Appendix B (Corollary B5), some connectivity of Granger causality may be missed if the Granger causality is estimated by the static MVAR model for the whole time series, due to the correlation of the causality measurement and the time-varying causal coefficients. We studied individually the correlations between the causality measurement, the sum of the absolute values of the estimated causal coefficients, and the absolute value of the sum of the estimated causal coefficients, across all time windows defined by the change-point set (S_t) in the TV-MVAR model. For 198 subjects, the absolute values of the median of this summation were plotted against the median of the Granger causality for each direction in Figure 7A. This correlation between average Granger causality and the sum of the causal coefficients decreased for finer time windows, compared with the classic Granger causality. In contrast, this correlation increased, if the absolute value of the median of the sum of the causal coefficients was considered (Figure 7B). As shown in Eq. (A2) in Appendix A, summing the causal coefficients may lead elimination of some positive causal influences with negative ones. In other words, the classic Granger causality, or Granger causality with coarser-scale tends to give null prediction when the sum of the causal coefficients is near to zero, but the zero sum may be given by the significant non-zero coefficients with different signs in different time windows.

The results for some particular examples were given in Figure 8. The classic Granger causality using the whole time series data gave near zero¹ causality measurements when the summations of the causal coefficients across all time windows were near to

¹The magnitude of the causality measurement is significantly larger than 0, if the lower bound of the 95% confidence interval of the causality in 198 subjects is greater than 0.0002 for the classical Granger causality and 0.0726 for the average Granger causality.

zero for the directions ‘Precuneus_R→Hippocampus_R’ and ‘Thalamus_R→Precuneus_L’. However, both the average Granger causality and the classic Granger causality detected significant causality for the other three directions, as shown in Figure 8, since the sum of the causal coefficients across all time windows were larger than zero.

2) Granger causality mapping from precuneus

The approaches were used to identify the Grange causality mapping from the precuneus, which was believed to be the core of many cognitive behaviours and self-consciousness and named “mind’s eye” (Cavanna and Trimble, 2006), to other brain regions. The proposed average Granger causality with optimal time-window dividing algorithm (AGC-OTWDA) was used for the resting state dataset by setting the maximum number of time-windows as 3. The significance of a causality influence was detected by the statistical test (See Material and Method). The analysis was also carried out for each subject by the classic Granger causality in contrast.

The classic Granger causality based on the whole time series failed to detect any significant² causal connectivity from the precuneus, while the AGC-OTWDA identified directional neural circuits centred at the precuneus, as shown in Figure 9. Since this data set was collected with the subjects’ eyes open, the information flows from the precuneus and the visual recognition network of brain regions were very significant, marked in green in Figure 9.

To ascertain that the relative variation of HRF is not a significant confounding factor for the results we got for the precuneus, the cross-correlation function between the BOLD signals of two regions in each causal connection was examined. The peaks of the cross-correlation function appeared at zero lag in more than 90% of the subjects for most of the pairs, except for the pairs between the right precuneus (PCUN.R), the

²A significant causality is identified if its *p*-value was less than 0.05 in at least 73% of the subjects.

right Precentral gyrus (preCG.R) and the opercular part of the right Inferior frontal gyrus (IFGoperc.R) had only 68% peaks at the zero lag. Therefore, the relative variation of HRF was not a significant factor in the causality results between the precuneus and the visual recognition network.

Validating Results on the Attention-Task fMRI Dataset

For the attention task, we were to detect the causality between rIPS and rTPJ. The Granger causalities were estimated for all possible pairs of voxels and averaged as the spatial Granger causality. Two ways were used to calculate the Granger causality. One was to concatenate the time series data in each attention block together into a long time series data, and then compute the Granger causality; the other was to calculate the Granger causality for each attention block and average them, i.e. the average Granger causality defined above. For comparison, we applied these two ways to estimate the Granger causality of two directions, rIPS→rTPJ and rTPJ→rIPS, for 12 subjects.

As shown in Figure 10, the average Granger causality is clearly larger than the classic Granger causality. For both directions, the differences between the causalities established by two different ways were calculated for all 12 subjects and the paired two-sample t-test was done to examine the difference, i.e., average Granger causality subtracting classic Granger causality. The right-tailed t-test suggested that the differences in both directions are significantly larger than 0 with the p -values equal to 6.6482×10^{-6} for rIPS→rTPJ and 9.0040×10^{-5} for rTPJ→rIPS, respectively. These results were consistent with our theoretical analysis, i.e. average Granger causality analysis across many shorter time series provided by multi-trials gives larger measurements than one long-term series observation can do.

Discussion

Danger of smoothing out causal information in long-term recordings

When we have long-term recordings of time series observation, how to reliably

estimate Granger causality between the time series? A naive and intuitive approach is to take all recordings into the MVAR model to estimate the Granger causality. This approach is based on the widely-accepted statistical belief that the more data are used, the closer the result will be to the true value. However, in this paper, our theoretical analysis and numerical examples demonstrate that this may not be the case in fMRI data analysis. The reliability of the statistical inference depends not only on how many data there are, despite its importance, but also how finely the model describes the data.

In this paper, we have discussed the effects of the fine-scaled details in the MVAR model on the Granger causality for detecting the directional information flows between time series data and applied the results to fMRI data analysis. This effect is mathematically analysed and it was concluded that both the temporal and the spatial characteristics of the MVAR model affect the reliability of the estimation of Granger causality. A smaller change-point set implied a coarser model and a larger one implies a finer model. As we proved, in the coarser model (with fewer change-points), the Granger causalities including both the cumulative and the average ones are smaller than that in a finer model (with more change-points). As demonstrated by the numerical simulations, the classic Granger causality becomes the lower bound of the average and the cumulative Granger causalities (Corollaries B2 and B5), while the causality established by using the real change-point set give the upper bound. Our results demonstrate that the Granger causality depends on the model configuration, thus “the devil is in the details”.

The Granger causality was proved to be equivalent to the transfer information (entropy) between Gaussian processes. It has been widely argued that the definition of the information strongly depends on the modelling configuration for the physical system (Jaynes, 1985). As argued by (Lloyd, 1989), the coarse-grained modelling (such as imperfectly determined evolution) may lead to information loss. Hence, the calculation of Granger causality or transfer information definitely suffers from the

issue of the modelling configuration.

Trade-off between preciseness of estimation and fineness of modelling

For a given data set, if we use too many change-points for the TV-MVAR model to have enough data points at each time window, we may get inaccurate estimation of the coefficients for the model. In other words, the larger change-point set implies a finer model (possibly a larger Granger causality) but may become an obstacle for the precise estimation of the Granger causality. Therefore, an optimal change-point set should be a trade-off between the preciseness of statistic estimation and the fineness of modelling. In this paper, we have proposed a novel algorithm for detecting the optimal change-point set based on the Bayesian information criterion (BIC). As illustrated by numerical simulation, this algorithm can correctly identify the change-points in the model and increase the reliability and significance for Granger causality analysis. However, compared to the models with time windows of equal lengths, the optimal time window dividing algorithm was time consuming. When we focus on the global index measuring the directed information flow instead of the exact evolution course of the underlying structure, the optimal time window can be determined by either the optimal time window dividing algorithm or by comparing the BIC's given by the models with equally divided time windows in different lengths.

Effects of HRF delay and down-sampling on the proposed methods

The effects of the HRF delay on the Granger causality analysis have been discussed by many researches. In this paper, we found that as the opposite delay increased the TP rate dropped down and the FP rate went up, and this result is consist to (Smith et al., 2012). In (Deshpande et al., 2010), the authors convolved the HRF with the local field potentials (LFP) recorded from the macaque, and found that even if the HRF delays as big as 2.5 seconds opposed the neuronal delays the minimum detectable neuronal delay was still in the order of a hundred milliseconds. Most recently, Schippers et al. (2011) did another simulation based investigation on the same issue and found that Granger causality can successfully detect over 80% of the cases when

the influences flowing to a region with a faster hemodynamic delay if the neuronal delays were above 1s. These results suggest that the Granger causality analysis (GCA) performs well when the HRF delay between regions is short, but when the HRF delay is long, additional procedures must be taken to minimize the effects of the HRF delay on the results given by GCA. In this paper, we have tried to de-convoluting the neuronal signal from the BOLD signal by an advanced Kalman filter (Havlicek et al., 2011), but no significant improvement was observed (data not shown). Assuming the regional HRF delay can be estimated accurately, the performance of the GCA can be improved by realigning the BOLD signals from two regions to control the HRF delay. Note that to make this realignment work requires the sampling rate of BOLD signal is finer than the HRF delay between two regions of interest. Typically, the TR of fMRI is 2~3 seconds for whole brain imaging, and by sacrificing the spatial coverage and spatial resolution the temporal resolution can be as high as 500 milliseconds (Arichi et al., 2012). Fortunately, the speed of fMRI has been developing rapidly (Feinberg and Yacoub, 2012), and the sub-second whole brain fMRI has already been available (Feinberg et al., 2010). In fact, the most recent advance in MRI technology enables the temporal resolution as fast as 50 milliseconds (Boyacioglu and Barth, 2012). Meanwhile, the accurate and robust estimation of HRF in BOLD signal has been a fundamental and hot issue for a long time in fMRI data analysis, and many estimating methods have been proposed, including the classical paper (Friston et al., 1994) and the most recent development (Wang et al., 2011) among many others. Therefore, the accurate estimation of regional HRF and the realignment of BOLD signal to correct the HRF delay are one of our future works for the GCA on fMRI data.

Comparison with filter based approaches

Considering the regional variation of HRF and physiological noise, we simulated the fMRI time series. Based on this dataset, we have compared the performances of the proposed optimal Granger causality (GC) approaches with the classic GC and the dual Kalman filter cumulative GC, and discussed the effect of the regional variation of HRF on the Granger causality analysis. The optimal GC approaches outperformed the

other two methods in this simulation. We do not mean by this example that our approaches MUST be better than the dual Kalman filter approach. However, this extension of our definition of GC to other approaches handling time-varying dynamics is definitely an interesting and important issue that would give a new insight to GC and time-varying dynamics theories. It should be one of our future research aims.

Precuneus plays as a hub in resting-state

For another resting-state fMRI data set, the proposed approach succeeded in detecting a number of Granger causal interdependencies from the precuneus to other brain regions, which cannot be inferred by the classic Granger causality, based on the static MVAR model for the whole BOLD time courses. In particular, a circuit centred at the precuneus to the visual network provided a proof of the pivotal role played by the precuneus in the visual cognition.

Possibility of detecting status change in fMRI data

In attention-task fMRI data, our approach with spatial-temporal finer-scale details detected the information transfer flows between the brain areas rIPS and rTPJ. A possible application for this method is detecting the status change in data. However, the experimental design in this study for the attention-task was a mixed blocked/ER design. For each subject and for each block, the stimuli were randomized (see experimental design). Responses were not required for all stimuli and therefore were randomized too. Both might impact the dynamics of the BOLD signal besides the block onset and block offset. That could cause detection of unpredictable change-points within the block. Therefore, the current experimental design is not optimal for this purpose. This could be a separate important issue. Additional experimental design efforts and method development may be needed in the future.

Further directions in spatio-temporal Granger causality algorithm

The proposed framework named the spatio-temporal Granger causality consists of

several modules, including the change-points detection, parameter estimation and number of change-points determination. We emphasize that the current algorithm is not the best one since more sophisticated method for each module may improve the overall performance of the analysis. Our future work will aim to search better algorithms for estimating more precise global Granger causality under the current framework, by using up-to-date approaches in each module and compare with the existing algorithms (Cribben et al., 2012; Havlicek et al., 2010; Hemmelmann et al., 2009; Hesse et al., 2003).

Conclusions

The estimation of Granger causality is heavily influenced by the model. Our results show that a coarse-grained approach/model may average out the meaningful information, for ‘the devil is in the details’. The widely held belief that better statistics (Granger causality) result from longer recording of the data set is not always true if the whole long-term time series is incorporated into the coarse-grained MVAR model. Instead, we suggest that the optimal strategy is to divide the long-term recording into a number of time windows by some optimal BIC-based algorithms. Reliable estimation of the Granger causality by a finer-scale MVAR model both in time and space can be achieved.

We have proposed a new framework of inferring Granger causality between groups of times series by taking the finer-scale details into the MVAR model. Our approach shows a good power to detect the information transfer between brain regions in fMRI BOLD signals and enhance the reliability of the estimation. This idea and approach may give rise to a new angle towards the debating of the reliability of Granger causality for fMRI data, in particular, resting-state fMRI time courses.

Acknowledgements

We acknowledge two anonymous reviewers for their insightful comments and suggestions. JF is a Royal Society Wolfson Research Merit Award holder, partially

supported by National Centre for Mathematics, Interdisciplinary Sciences (NCMIS) of the Chinese Academy of Sciences and the Key Program of National Natural Science Foundation of China (No. 91230201). QL is partially supported by grant from the National Natural Sciences Foundation of China (No. 11101429, 11271121), Research Fund for the Doctoral Program of Higher Education of China (No. 20114307120019), and the National Basic Research Program of China (No. 2011CB707802). LWL is jointly supported by the Marie Curie International Incoming Fellowship from the European Commission (FP7-PEOPLE-2011-IIF-302421), the National Natural Sciences Foundation of China (No. 61273309), the Foundation for the Author of National Excellent Doctoral Dissertation of PR China (No. 200921), Shanghai Rising-Star Program (No. 11QA1400400), and also by the Laboratory of Mathematics for Nonlinear Science, Fudan University.

Appendix A: Solution of the time-varying linear regression.

To build up a theoretical analysis of the Granger causality, we assume that the time series are *generated* by the following the first-order (discrete-time) time-varying multivariate autoregressive (TV-MVAR) model:

$$x^{(t+1)} = a_1(t)x^t + b_1(t)y^t + n(t), t = 1, 2, \dots, T, \quad (\text{A1})$$

where n_t is white Gaussian noise statistically independent of x and y :

$$E n(t) = 0, \quad E[n(t)n(t')] = \sigma_n^2(t)\delta_{t,t'}.$$

Here, $\delta_{t,t'}$ is the Kronecker delta. Without loss of generality, we can suppose that x^t and y^t are centred, *i.e.*, all means are equal to zeros, and the variances of x^t and y^t both equal to 1, by multiplying coefficients $a_1(t)$ and $b_1(t)$ by their variances, respectively. Moreover, we assume that the correlation between x^t and y^t are stationary, *i.e.*, $E(x^t y^t) = c$ for a constant $c \in [0, 1]$. Thus, we can perform a simple linear transformation to make x and y orthogonal:

$$z^t = \frac{(y^t - cx^t)}{\sqrt{1-c^2}},$$

which implies that z^t has its mean equal to 0 and its variance equal to 1, and is uncorrelated with x^t . Thus, (A1) becomes:

$$x^{t+1} = \tilde{a}_1(t)x^t + \tilde{b}_1(t)z^t + n^t$$

with $\tilde{a}_1(t) = a_1(t) + b_1(t)c$, $\tilde{b}_1(t) = b_1(t)\sqrt{1-c^2}$. Hence, we can discuss this problem by assuming x^t and y^t are uncorrelated that will not lose generality. Therefore, in the following, we keep assuming x^t and y^t are uncorrelated.

Considering the time-varying linear regression system (A1), we estimate the Granger causality with different time-window split. More generally, we consider (2) or (3) to replace the intrinsic system. To estimate the **theoretical** values of the time-varying Granger causalities by averaging or cumulating as mentioned in the main text, first, we are to estimate the parameters $\bar{a}_1^{S_1}(k)$ and $\bar{b}_1^{(S_1)}(k)$ by minimizing the following residual square errors across the whole time interval:

$$\begin{aligned} & \sum_{t=1}^T E \left[\left(x^{t+1} - \bar{a}_1^{S_1}(k)x^t - \bar{b}_1^{S_1}(k)y^t \right)^2 \right] \\ &= \sum_{t=1}^T E \left\{ \left[\left(a_1(t) - \bar{a}_1^{S_1}(k) \right) x^t + \left(b_1(t) - \bar{b}_1^{S_1}(k) \right) y^t + n^t \right]^2 \right\} \\ &= \sum_{k=1}^m \sum_{t=t_{k-1}}^{t_k-1} E \left\{ \left[\left(a_1(t) - \bar{a}_1^{S_1}(k) \right) x^t + \left(b_1(t) - \bar{b}_1^{S_1}(k) \right) y^t + n^t \right]^2 \right\} \\ &= \sum_{k=1}^m \sum_{t=t_{k-1}}^{t_k-1} \left[\left(a_1(t) - \bar{a}_1^{S_1}(k) \right)^2 + \left(b_1(t) - \bar{b}_1^{S_1}(k) \right)^2 + \sigma_n^2(t) \right] \end{aligned}$$

which is equivalent to a series of minimisation problems:

$$\min_{\bar{a}_1^{S_1}(k)} \sum_{t=t_{k-1}}^{t_k-1} \left(a_1(t) - \bar{a}_1^{S_1}(k) \right)^2, \quad \min_{\bar{b}_1^{S_1}(k)} \sum_{t=t_{k-1}}^{t_k-1} \left(b_1(t) - \bar{b}_1^{S_1}(k) \right)^2$$

for all $k = 1, \dots, m$. It can be seen that the (expectation of) the solution should be

$$\bar{a}_1^{S_1}(k) = \frac{1}{t_k - t_{k-1}} \sum_{t=t_{k-1}}^{t_k-1} a_1(t), \quad \bar{b}_1^{S_1}(k) = \frac{1}{t_k - t_{k-1}} \sum_{t=t_{k-1}}^{t_k-1} b_1(t), \quad \text{for all } k. \quad (\text{A2})$$

Appendix B: Monotonicity of the Ganger causalities of TV-MVAR models

Monotonicity of cumulative Granger causality.

By the estimation of the coefficients, Eq. (A2), the cumulative Granger causality with the given time window lengths can be estimated as:

$$F_{Y \rightarrow X}^{(c, S_1)} = \log \left(\frac{U_{S_1} + \sum_{t=1}^T (b_1(t))^2 + \sum_{t=1}^T \sigma_n^2(t)}{U_{S_1} + V_{S_1} + \sum_{t=1}^T \sigma_n^2(t)} \right),$$

where

$$U_{S_1} = \sum_{k=1}^m \sum_{t=t_{k-1}}^{t_k-1} (a_1(t) - \bar{a}_1^{S_1}(k))^2, \quad V_{S_1} = \sum_{k=1}^m \sum_{t=t_{k-1}}^{t_k-1} (b_1(t) - \bar{b}_1^{S_1}(k))^2.$$

We have the following result.

Theorem B1. For two change-point sets S_1 and S_2 , if $S_1 \subseteq S_2$, then

$$F_{Y \rightarrow X}^{(c, S_1)} \leq F_{Y \rightarrow X}^{(c, S_2)}$$

Proof. Let S_1 be composed of the following integer series:

$$1 = t_0 < t_1 < \dots < t_{m-1} < t_m = T + 1$$

Since the increasing integer series S_2 contains S_1 , we can denote S_2 as follows;

$$\begin{aligned} 1 = (t_0 =) t_1^1 < t_1^2 < \dots < t_1^{n_1} < t_1^{n_1+1} = t_2^1 (= t_1) \\ < \dots < t_{m-1}^{n_{m-1}+1} = t_m^1 (= t_{m-1}) < t_m^2 < \dots < t_m^{n_m} (= t_m) = T + 1. \end{aligned}$$

In other words, in each time interval defined by S_1 , for instance, from t_{k-1} to t_k , we

denote $t_k^1 < t_k^2 < \dots < t_k^{n_k} < t_k^{n_k+1}$ as the integers in S_2 , which are located between t_{k-1}

and t_k . For simplicity, we let $t_k^{n_k+1} = t_{k+1}^1$. Then, the TV-MVAR model with respect to

S_2 can be formulated as

$$x^{t+1} = \bar{a}_1^{S_2}(k, q) x^t + \bar{b}_1^{S_2}(k, q) x^t + \tilde{n}(t),$$

$$t_k^q \leq t < t_k^{q+1}, q = 1, \dots, n_k, k = 1, \dots, m. \quad (B1)$$

First, we are to prove that $U_{S_1} \geq U_{S_2}$ and $V_{S_1} \geq V_{S_2}$ that are essentially the same. So,

we need to prove one of them, for instance, $V_{S_1} \geq V_{S_2}$.

In fact, we rewrite V_{S_2} as follows:

$$V_{S_2} = \sum_{k=1}^{|S_1|} \sum_{q=1}^{n_k} \sum_{t=t_k^q}^{t_k^{q+1}-1} \left(b_1(t) - \bar{b}_1^{S_2}(\tau(t_k^q)) \right)^2$$

where $\tau(t_k^q)$ denotes the order of t_k^q in the ordered integer set S_2 .

Thus, it is sufficient to show that in each time window of S_1 , it holds that

$$\sum_{t=t_{k-1}}^{t_k-1} \left(b_1(t) - \bar{b}_1^{S_1}(k) \right)^2 \geq \sum_{q=1}^{n_k} \sum_{t=t_k^q}^{t_k^{q+1}-1} \left(b_1(t) - \bar{b}_1^{S_2}(\tau(t_k^q)) \right)^2.$$

We note that

$$\begin{aligned} \sum_{t=t_{k-1}}^{t_k-1} \left(b_1(t) - \bar{b}_1^{S_1}(k) \right)^2 &= \sum_{t=t_{k-1}}^{t_k-1} [b_1(t)]^2 - (t_k - t_{k-1}) [\bar{b}_1^{S_1}(k)]^2, \\ \sum_{q=1}^{n_k} \sum_{t=t_k^q}^{t_k^{q+1}-1} \left(b_1(t) - \bar{b}_1^{S_2}(\tau(t_k^q)) \right)^2 &= \sum_{t=t_{k-1}}^{t_k-1} b_1^2(t) - \sum_{q=1}^{n_k} (t_k^{q+1} - t_k^q) \left(\bar{b}_1^{S_2}(\tau(t_k^q)) \right)^2 \end{aligned}$$

and

$$\bar{b}_1^{S_1}(k) = \frac{1}{t_k - t_{k-1}} \sum_{q=1}^{n_k} (t_k^{q+1} - t_k^q) \bar{b}_1^{S_2}(\tau(t_k^q)), \quad \sum_{q=1}^{n_k} (t_k^{q+1} - t_k^q) = t_k - t_{k-1}.$$

Hence,

$$\begin{aligned} &(t_k - t_{k-1}) [\bar{b}_1^{S_1}(k)]^2 \\ &= (t_k - t_{k-1}) \left[\frac{1}{t_k - t_{k-1}} \sum_{q=1}^{n_k} (t_k^{q+1} - t_k^q) \bar{b}_1^{S_2}(\tau(t_k^q)) \right]^2 \\ &\leq (t_k - t_{k-1}) \frac{1}{t_k - t_{k-1}} \sum_{q=1}^{n_k} (t_k^{q+1} - t_k^q) [\bar{b}_1^{S_2}(\tau(t_k^q))]^2 \\ &= \sum_{q=1}^{n_k} (t_k^{q+1} - t_k^q) [\bar{b}_1^{S_2}(\tau(t_k^q))]^2 \end{aligned} \tag{B2}$$

owing to the well-known fact that the weighted algebraic average is less than the square average with the weighting. This implies $V_{S_1} \geq V_{S_2}$. So, it is with $U_{S_1} \geq U_{S_2}$.

From $V_{S_1} \geq V_{S_2}$, we immediately have

$$\frac{\sum_{t=1}^T (b_1(t))^2 + \sum_{t=1}^T \sigma_n^2(t)}{V_{S_1} + \sum_{t=1}^T \sigma_n^2(t)} \leq \frac{\sum_{t=1}^T (b_1(t))^2 + \sum_{t=1}^T \sigma_n^2(t)}{V_{S_2} + \sum_{t=1}^T \sigma_n^2(t)}$$

Combined by $U_{S_1} \geq U_{S_2}$, we can derive

$$\frac{U_{S_1} + \sum_{t=1}^T (b_1(t))^2 + \sum_{t=1}^T \sigma_n^2(t)}{U_{S_1} + V_{S_1} + \sum_{t=1}^T \sigma_n^2(t)} \leq \frac{U_{S_2} + \sum_{t=1}^T (b_1(t))^2 + \sum_{t=1}^T \sigma_n^2(t)}{U_{S_2} + V_{S_2} + \sum_{t=1}^T \sigma_n^2(t)}$$

This means $F_{Y \rightarrow X}^{(c, S_1)} \leq F_{Y \rightarrow X}^{(c, S_2)}$. From (B2), one can see that the inequality holds if and only if

$$\bar{b}_1^{S_2}(\tau(t_k^q)) = \bar{b}_1^{S_1}(k) \quad (\text{B3})$$

holds for all $q = 1, \dots, n_k$ and all k . □

From Theorem B1 and its proof, in particular Eq. (B3) as the sufficient and necessary condition for $F_{Y \rightarrow X}^{(c, S_1)} = F_{Y \rightarrow X}^{(c, S_2)}$. We immediately have the upper and lower bounds of the cumulative Granger causality.

Corollary B2. Let $S_0 = \{1, T+1\}$ and S_* be the ordered time point set that exactly comprise of the change-points in the TV-MVAR. Then, for any ordered time point set S , we have

$$F_{Y \rightarrow X}^{(c, S_0)} \leq F_{Y \rightarrow X}^{(c, S)} \leq F_{Y \rightarrow X}^{(c, S_*)}$$

This corollary shows that the static (classic) Granger causality actually is the lower-bound of the cumulative Granger causality. And, if the time series are exactly generated by TV-MVAR (A1) with the change-point set S_* , the cumulative Granger causality based on it is the upper bounds of all.

We should point out that Theorem B1 holds under the condition that one switching time set is contained in the other. It does not imply that the more change-points are, the larger cumulative Granger causality it will have.

Conjecture 1. If $|S_2| \geq |S_1|$, then $F_{Y \rightarrow X}^{(c, S_1)} \leq F_{Y \rightarrow X}^{(c, S_2)}$.

We claim that this conjecture is **not true** by a simple counter example. Let $T = 6$, $S_1 = \{1, 4, 7\}$, $S_2 = \{1, 3, 5, 7\}$, and $S = \{1, 7\}$. We suppose that the data is produced by the model (5) with a constant a_1 and $b_1(t)$ is periodic with a period 2, i.e.,

$b_1(1) = b_1(3) = b_1(5)$ and $b_1(2) = b_1(4) = b_1(6)$. But the two values do not equal pair-wisely. It is clear that for S_2 , the parameters can be estimated as

$$\bar{b}_1^{S_2}(1) = \bar{b}_1^{S_2}(2) = \bar{b}_1^{S_2}(3) = \frac{1}{2}(b_1(1) + b_1(2)),$$

which equals to the whole average

$$\bar{b}_1 = \frac{1}{6}(b_1(1) + b_1(2) + b_1(3) + b_1(4) + b_1(5) + b_1(6)).$$

So, the corresponding Granger Causality with S_2 can be estimated equal to that of the static MVAR model (the change-point is composed of S), i.e., $F_{Y \rightarrow X}^{(c, S_2)} = F_{Y \rightarrow X}^{(c, S)}$.

Noting that $F_{Y \rightarrow X}^{(c, S)} < F_{Y \rightarrow X}^{(c, S_1)}$, where the strict inequality is because of

$$\bar{b}_1^{S_1}(1) = \frac{1}{3}(b_1(1) + b_1(2) + b_3(2)) \neq \bar{b}_1. \text{ So, we have } F_{Y \rightarrow X}^{(c, S_2)} < F_{Y \rightarrow X}^{(c, S_1)} \text{ despite } |S_2| > |S_1|.$$

Let us consider a numerical example with $a_1(t) = 1$, $\sigma_n^1(t) = 1$ for all t , and

$b_1(1) = b_1(3) = b_1(5) = 1$ and $b_1(2) = b_1(4) = b_1(6) = 0$. Direct calculations lead that

$$\begin{aligned} F_{Y \rightarrow X}^{(c, S_1)} &= \log \left(\frac{\sum_{t=1}^6 (b_1(t))^2 + 6}{\sum_{k=1}^2 \sum_{t=3(k-1)+1}^{3k} (b_1(t) - \bar{b}_1^i(k))^2 + 6} \right) \\ &= \log \frac{6+3}{8/9+6} = \log \frac{81}{62}. \end{aligned}$$

However,

$$\begin{aligned} F_{Y \rightarrow X}^{(c, S_2)} &= \log \left(\frac{\sum_{t=1}^6 (b_1(t))^2 + 6}{\sum_{k=1}^3 \sum_{t=2(k-1)+1}^{2k} (b_1(t) - \bar{b}_1^i(k))^2 + 6} \right) \\ &= \log \frac{6+3}{3/2+6} = \log \frac{6}{5} < \log \frac{81}{62} = F_{Y \rightarrow X}^{(c, S_1)}. \end{aligned}$$

Monotonicity of average Granger causality.

Another approach to estimate the Granger causality of TV-MVAR model is to estimate the Granger causality at each time windows (between switching) can average them according to the length of each time window. Recall $S_1 = \{1 = t_0 < t_1 < \dots < t_{m-1} < t_m = T + 1\}$ as an increasing integer sequence that denote the change-point and the TV-MVAR model as

$$x^{t+1} = \bar{a}_1^{S_1}(k)x^t + \bar{b}_1^{S_1}(k)x^t + \bar{n}(t), t_{k-1} \leq t < t_k, k = \dots, m \quad (\text{B4})$$

At each time window, the Granger causality can be estimated as

$$F_{Y \rightarrow X}^{(k, S_1)} = \log \left(\frac{U_k + \sum_{t=t_{k-1}}^{t_k-1} (b_1(t))^2 + \sum_{t=t_{k-1}}^{t_k-1} \sigma_n^2(t)}{U_k + V_k + \sum_{t=t_{k-1}}^{t_k-1} \sigma_n^2(t)} \right)$$

With

$$U_k = \sum_{t=t_{k-1}}^{t_k-1} (a_1(t) - \bar{a}_1^{S_1}(k))^2, V_k = \sum_{t=t_{k-1}}^{t_k-1} (b_1(t) - \bar{b}_1^{S_1}(k))^2.$$

Then, we estimate the Granger Causality by the TV-MVAR model (B4) as follows:

$$F_{Y \rightarrow X}^{(a, S_1)} = \frac{1}{T} \sum_{k=1}^m F_{Y \rightarrow X}^{(k, S_1)}(t_k - t_{k-1}),$$

denoted by the average Granger causality, the weighted average according to the lengths of the time windows. To investigate the relationship of the average Granger causality, we need the following lemma:

Lemma B3. For any positive integer T , any m real constants $[c_t]_{t=1}^T$, any T

nonnegative constants $[p_t]_{t=1}^T$ with $\sum_{t=1}^T p_t = 1$ and any positive constants $[\sigma_t^2]_{t=1}^T$,

we have the following inequality

$$\log \left(\frac{\sum_{t=1}^T c_t^2 p_t + \sigma^2}{\sum_{t=1}^T (c_t - \bar{c})^2 p_t + \sigma^2} \right) \leq \sum_{t=1}^T p_t \log \left(\frac{c_t^2 + \sigma_t^2}{\sigma_t^2} \right)$$

where $\bar{c} = \sum_{t=1}^T p_t c_t$ and $\sigma^2 = \sum_{t=1}^T p_t \sigma_t^2$.

Proof. Let us consider the following function with respect to $C = [c_t]_{t=1}^T$ and

$$\Sigma = [\sigma_t^2]_{t=1}^T$$

$$V = \log \frac{\sigma^2 + c^2}{\sigma^2 + v} - \sum_{t=1}^T p_t \log \left(\frac{\sigma_t^2 + c_t^2}{\sigma_t^2} \right)$$

with

$$c^2 = \sum_{t=1}^T c_t^2 p_t, v = \sum_{t=1}^T [c(t) - \bar{c}]^2 p_t = c^2 - (\bar{c})^2.$$

We make minor modifications on the problem according to the following three facts.

First, noting

$$v = \sum_{t=1}^T [c_t - \bar{c}]^2 p_t = \sum_{t=1}^T [c_t]^2 p_t - \left(\sum_{t=1}^T c_t p_t \right)^2 \geq \sum_{t=1}^T |c_t|^2 p_t - \left(\sum_{t=1}^T |c_t| p_t \right)^2,$$

if we replace c_t by $|c_t|$ in V , which is denoted by \hat{V} , then we have $V \leq \hat{V}$.

Therefore, without loss of generality, it is sufficient to prove $\hat{V} \leq 0$ by considering the case that all c_t are nonnegative.

Second, considering

$$\left. \frac{\partial V}{\partial c_t} \right|_{c_t=0} = \frac{2\bar{c}p_t}{\sigma^2 + v},$$

which is positive in the case that there is at least one positive c_t with nonzero p_t . So, it is sufficient to consider the case that all c_t are positive;

Third, it holds

$$\sum_{t=1}^T p_t \log(\sigma_t^2) \leq \log(\sigma^2)$$

owing to the Jensen's inequality.

In summary, we can consider the following function instead of V :

$$\tilde{V}(y, v, \Sigma) = \log \frac{\sigma^2 + c^2}{\sigma^2 + v} - \sum_{t=1}^T p_t \log \left(\frac{\sigma_t^2 + y_t}{\sigma^2} \right).$$

Letting $y_t = (c_t)^2$, owing to the fact that all c_t are nonnegative, $y = [y_t]$, with fixed c^2 and σ^2 , we are going to show that \tilde{V} is nonnegative by considering the following maximization problem:

$$\max \tilde{V}(y, v, \Sigma)$$

$$\text{s.t. } \sum_{t=1}^T y_t p_t = c^2, \sum_{t=1}^T \sqrt{y_t} p_t = \sqrt{c^2 - v}, \sum_{t=1}^T p_t \sigma_t^2 = \sigma^2, \sigma_t^2 > 0, y_t > 0, \forall t \quad (\text{B5})$$

To solve (B5), we introduce the following auxiliary Lagrange function:

$$\begin{aligned}
& L(y, v, \Sigma, \lambda, \mu, \gamma) \\
& = \tilde{V}(y, v, \Sigma) + \lambda \left(\sum_{t=1}^T y_t p_t - b^2 \right) + \mu \left(\sum_{t=1}^T \sqrt{y_t} p_t - \sqrt{c^2 - v} \right) + \gamma \left(\sum_{t=1}^T \sigma_t^2 p_t - \sigma^2 \right)
\end{aligned}$$

By the Karush-Kuhn-Tucker conditions, the necessary conditions of the minimum of (B5) include:

$$\frac{\partial L}{\partial y_t} = p_t \left[-\frac{1}{(\sigma_t^2 + y_t)} + \lambda + \frac{\mu}{2\sqrt{y_t}} \right] = 0,$$

$$\frac{\partial L}{\partial v} = -\frac{1}{\sigma^2 + v} + \frac{\mu}{2\sqrt{c^2 - v}} = 0,$$

$$\frac{\partial L}{\partial (\sigma_t^2)} = p_t \left[-\frac{1}{(\sigma_t^2 + y_t)} + \gamma \right] = 0$$

This leads (i) $p_t = 0$ or (ii) $\sigma_t^2 + y_t = 1/\gamma$ and

$$y_t = \left[\frac{\mu}{2(\gamma - \lambda)} \right]^2. \quad (\text{B6})$$

In other words, for these y_t with nonzero p_t , if we are to solve y_t from the above equalities as a function with respect to $\sigma, \lambda, \mu, \gamma, c^2$ and v , which are independent of the index t , then we can only have one expression from (B6). It should be emphasized that we are not solving the values of y_t but its expression with respect to the t -independent quantities, $\sigma, \lambda, \mu, \gamma, c^2$ and v . Therefore, the possible minimum points of $R(y, v)$ only has one single value of y_t . So it is with

$$\sigma_t^2 = \frac{1}{\gamma} - \left[\frac{\mu}{2(\gamma - \lambda)} \right]^2$$

It can be seen that if y_t and σ_t^2 can only have a single value respectively, then $\tilde{V}(y, v, \Sigma) = 0$. So, the maximum of $\tilde{V}(y, v, \Sigma)$ is zero. Hence, the intrinsic V has its maximum equal to zero. Therefore, lemma B2 is proved and the equality holds if and only if y_t and σ_t^2 can only have a single value respectively. \square

Theorem B4. Let S_1 and S_2 be two sequences of increasing integers. If $S_1 \subseteq S_2$, then

$$F_{Y \rightarrow X}^{(a, S_1)} \leq F_{Y \rightarrow X}^{(a, S_2)}.$$

Proof. We denote the sets S_1 and S_2 by the symbols as in the proof of Theorem B1.

According to (B1), the Granger causality at the time window of S_2 , the k -th window of S_1 and the q -th can be written as:

$$F_{Y \rightarrow X}^{(k, q, S_2)} = \log \left(\frac{U_{k, q} + \sum_{t=t_k^q}^{t_k^{q+1}-1} (b_1(t))^2 + \sum_{t=t_k^q}^{t_k^{q+1}-1} \sigma_n^2(t)}{U_{k, q} + V_{k, q} + \sum_{t=t_k^q}^{t_k^{q+1}-1} \sigma_n^2(t)} \right)$$

where

$$U_{k, q} = \sum_{t=t_k^q}^{t_k^{q+1}-1} (a_1(t) - \bar{a}_1^{S_2}(\tau(t_k^q)))^2, V_{k, q} = \sum_{t=t_k^q}^{t_k^{q+1}-1} (b_1(t) - \bar{b}_1^{S_2}(\tau(t_k^q)))^2.$$

Then, the average Granger causality with respect to S_2 is

$$F_{Y \rightarrow X}^{(a, S_2)} = \frac{1}{T} \sum_{k=1}^{|S_1|} \sum_{q=1}^{n_k} F_{Y \rightarrow X}^{(k, q, S_2)} (t_k^{q+1} - t_k^q).$$

Note

$$\sum_{q=1}^{n_k} \bar{a}_1^{S_2}(\tau(t_k^q)) (t_k^{q+1} - t_k^q) = \bar{a}_1^{S_1}(k), \sum_{q=1}^{n_k} \bar{b}_1^{S_2}(\tau(t_k^q)) (t_k^{q+1} - t_k^q) = \bar{b}_1^{S_1}(k),$$

and

$$\begin{aligned} \sum_{t=t_k^q}^{t_k^{q+1}-1} [a_1(t)]^2 &= \sum_{t=t_k^q}^{t_k^{q+1}-1} [a_1(t) - \bar{a}_1^{S_2}(\tau(t_k^q))]^2 + [\bar{a}_1^{S_2}(\tau(t_k^q))]^2 (t_k^{q+1} - t_k^q), \\ \sum_{t=t_k^q}^{t_k^{q+1}-1} [b_1(t)]^2 &= \sum_{t=t_k^q}^{t_k^{q+1}-1} [b_1(t) - \bar{b}_1^{S_2}(\tau(t_k^q))]^2 + [\bar{b}_1^{S_2}(\tau(t_k^q))]^2 (t_k^{q+1} - t_k^q). \end{aligned}$$

Compared with $F_{Y \rightarrow X}^{(a, S_2)}$, we can rewrite the term of $F_{Y \rightarrow X}^{(a, S_1)}$, i.e., $F_{Y \rightarrow X}^{(k, S_1)}$, as follows:

$$\begin{aligned}
F_{Y \rightarrow X}^{(k, S_1)} &= \log \left(\frac{U_k + \sum_{t=t_{k-1}}^{t_k-1} (b_1(t))^2 + \sum_{t=t_{k-1}}^{t_k-1} \sigma_n^2(t)}{U_k + V_k + \sum_{t=t_{k-1}}^{t_k-1} \sigma_n^2(t)} \right) \\
&= \log \left(\sum_{q=1}^{n_k} \left[\bar{a}_1^{S_1}(k) - \bar{a}_1^{S_2}(\tau(t_k^q)) \right]^2 (t_k^{q+1} - t_k^q) \right. \\
&\quad \left. + \sum_{q=1}^{n_k} \left[\bar{b}_1^{S_2}(\tau(t_k^q)) \right]^2 (t_k^{q+1} - t_k^q) + \sum_{q=1}^{n_k} \varepsilon_n^2(q) (t_k^{q+1} - t_k^q) \right) \\
&\quad - \log \left(\sum_{q=1}^{n_k} \left[\bar{a}_1^{S_1}(k) - \bar{a}_1^{S_2}(\tau(t_k^q)) \right]^2 (t_k^{q+1} - t_k^q) \right. \\
&\quad \left. + \sum_{q=1}^{n_k} \left[\bar{b}_1^{S_1}(k) - \bar{b}_1^{S_2}(\tau(t_k^q)) \right]^2 (t_k^{q+1} - t_k^q) + \sum_{q=1}^{n_k} \varepsilon_n^2(q) (t_k^{q+1} - t_k^q) \right)
\end{aligned}$$

where

$$\varepsilon_n^2(q) = \frac{1}{t_k^{q+1} - t_k^q} \sum_{t=t_k^q}^{t_k^{q+1}-1} \left\{ \left[a_1(t) - \bar{a}_1^{S_2}(\tau(t_k^q)) \right]^2 + \left[b_1(t) - \bar{b}_1^{S_2}(\tau(t_k^q)) \right]^2 + \sigma_n^2(t) \right\}.$$

Since

$$\begin{aligned}
&\frac{\sum_{q=1}^{n_k} \left[\bar{a}_1^{S_1}(k) - \bar{a}_1^{S_2}(\tau(t_k^q)) \right]^2 (t_k^{q+1} - t_k^q) + \sum_{q=1}^{n_k} \left[\bar{b}_1^{S_2}(\tau(t_k^q)) \right]^2 (t_k^{q+1} - t_k^q) + \sum_{q=1}^{n_k} \varepsilon_n^2(q) (t_k^{q+1} - t_k^q)}{\sum_{q=1}^{n_k} \left[\bar{a}_1^{S_1}(k) - \bar{a}_1^{S_2}(\tau(t_k^q)) \right]^2 (t_k^{q+1} - t_k^q) + \sum_{q=1}^{n_k} \left[\bar{b}_1^{S_1}(k) - \bar{b}_1^{S_2}(\tau(t_k^q)) \right]^2 (t_k^{q+1} - t_k^q) + \sum_{q=1}^{n_k} \varepsilon_n^2(q) (t_k^{q+1} - t_k^q)} \\
&\leq \frac{\sum_{q=1}^{n_k} \left[\bar{b}_1^{S_2}(\tau(t_k^q)) \right]^2 (t_k^{q+1} - t_k^q) + \sum_{q=1}^{n_k} \varepsilon_n^2(q) (t_k^{q+1} - t_k^q)}{\sum_{q=1}^{n_k} \left[\bar{b}_1^{S_1}(k) - \bar{b}_1^{S_2}(\tau(t_k^q)) \right]^2 (t_k^{q+1} - t_k^q) + \sum_{q=1}^{n_k} \varepsilon_n^2(q) (t_k^{q+1} - t_k^q)}
\end{aligned}$$

Theorem B3 can be derived by directly employing Lemma B3. In addition, the inequality holds if and only if $\bar{b}_1^{S_2}(\tau(t_k^q))$ and $\varepsilon_n^2(q)$ can only pick values independent of the index q (but possibly depending on the index k), respectively. \square

Similar to Corollary B2, from Theorem B4 and its proof, in particular the sufficient and necessary condition for $F_{Y \rightarrow X}^{(a, S_1)} = F_{Y \rightarrow X}^{(a, S_2)}$. We immediately have the upper and lower bounds of the cumulative Granger causality.

Corollary B5. Let $S_0 = \{1, T+1\}$ and S_* be the ordered time point set that exactly comprise of the change-points in the TV-MVAR model. Then, for any ordered time point set S , we have

$$F_{Y \rightarrow X}^{(a, S_0)} \leq F_{Y \rightarrow X}^{(a, S)} \leq F_{Y \rightarrow X}^{(a, S_*)}.$$

This corollary shows that the static (classic) Granger causality actually is the lower-bound of the average Granger causality. And, if the time series are exactly generated by TV-MVAR (A1) with the change-point set S_* , the average Granger causality based on it is the upper bounds of all.

We should also emphasize that the following conjecture is *not true*.

Conjecture B2. If $|S_2| \geq |S_1|$, then $F_{Y \rightarrow X}^{(a, S_1)} \leq F_{Y \rightarrow X}^{(a, S_2)}$.

That is to say, the average Granger causality is monotonic with respect to the containing relation between the change-point set, but not monotonic with respect to the size of the change-point sets. A counter-example can be easily established by the same way as in Remark 1.

Appendix C: Comparison between cumulative and average Ganger causalities

Magnitude comparison.

Actually, the two sorts of Granger causalities of the TV-MVAR model do not have definite magnitude relation. First, we show in the following theorem, the relation that cumulative Granger causality is greater than the average Granger causality with the same change-point set is **conditional**.

Theorem C1. Let S be a sequence of increasing integers. If the following quantity

$$\frac{1}{t_k - t_{k-1}} \left[\sum_{t=t_{k-1}}^{t_k-1} (a_1(t) - \bar{a}_1(k))^2 + \sum_{t=t_{k-1}}^{t_k-1} (b_1(t) - \bar{b}_1(k))^2 + \sum_{t=t_{k-1}}^{t_k-1} \sigma_n^2(t) \right]$$

With

$$\bar{a}_1(k) = \frac{1}{t_k - t_{k-1}} \sum_{t=t_{k-1}}^{t_k-1} a_1(t), \bar{b}_1(k) = \frac{1}{t_k - t_{k-1}} \sum_{t=t_{k-1}}^{t_k-1} b_1(t)$$

is independent of the index k , then

$$F_{Y \rightarrow X}^{(a, S)} \leq F_{Y \rightarrow X}^{(c, S)}.$$

Proof. Let $S = \{1 = t_0 < t_1 < \dots < t_{m-1} < t_m = T + 1\}$. And, with the same notations we used above, we have

$$F_{Y \rightarrow X}^{(c,S)} = \log \left(\frac{\sum_{k=1}^m \sum_{t=t_{k-1}}^{t_k-1} (a_1(t) - \bar{a}_1(k))^2 + \sum_{t=1}^T (b_1(t))^2 + \sum_{t=1}^T \sigma_n^2(t)}{\sum_{k=1}^m \sum_{t=t_{k-1}}^{t_k-1} (a_1(t) - \bar{a}_1(k))^2 + \sum_{k=1}^m \sum_{t=t_{k-1}}^{t_k-1} (b_1(t) - \bar{b}_1(k))^2 + \sum_{t=1}^T \sigma_n^2(t)} \right),$$

and

$$F_{Y \rightarrow X}^{(a,S)} = \frac{1}{T} \sum_{k=1}^m (t_k - t_{k-1}) \log \left(\frac{\sum_{t=t_{k-1}}^{t_k-1} (a_1(t) - \bar{a}_1(k))^2 + \sum_{t=t_{k-1}}^{t_k-1} (b_1(t))^2 + \sum_{t=t_{k-1}}^{t_k-1} \sigma_n^2(t)}{\sum_{t=t_{k-1}}^{t_k-1} (a_1(t) - \bar{a}_1(k))^2 + \sum_{t=t_{k-1}}^{t_k-1} (b_1(t) - \bar{b}_1(k))^2 + \sum_{t=t_{k-1}}^{t_k-1} \sigma_n^2(t)} \right)$$

Let $\bar{b}_1 = \frac{1}{T} \sum_{t=1}^T b_1(t)$. Thus, we can rewrite them as

$$F_{Y \rightarrow X}^{(c,S)} = \log \left(\frac{\sum_{k=1}^m \sum_{t=t_{k-1}}^{t_k-1} (a_1(t) - \bar{a}_1(k))^2 + \sum_{t=1}^m (\bar{b}_1(k))^2 (t_k - t_{k-1}) + \sum_{t=1}^m \sum_{t=t_{k-1}}^{t_k-1} (b_1(t) - \bar{b}_1(k))^2 + \sum_{t=1}^T \sigma_n^2(t)}{\sum_{k=1}^m \sum_{t=t_{k-1}}^{t_k-1} (a_1(t) - \bar{a}_1(k))^2 + \sum_{k=1}^m \sum_{t=t_{k-1}}^{t_k-1} (b_1(t) - \bar{b}_1(k))^2 + \sum_{t=1}^T \sigma_n^2(t)} \right)$$

and

$$F_{Y \rightarrow X}^{(a,S)} = \frac{1}{T} \sum_{k=1}^m (t_k - t_{k-1}) \times \log \left(\frac{\sum_{t=t_{k-1}}^{t_k-1} (a_1(t) - \bar{a}_1(k))^2 + \sum_{t=t_{k-1}}^{t_k-1} (b_1(t) - \bar{b}_1(k))^2 + (\bar{b}_1(k))^2 (t_k - t_{k-1}) + \sum_{t=t_{k-1}}^{t_k-1} \sigma_n^2(t)}{\sum_{t=t_{k-1}}^{t_k-1} (a_1(t) - \bar{a}_1(k))^2 + \sum_{t=t_{k-1}}^{t_k-1} (b_1(t) - \bar{b}_1(k))^2 + \sum_{t=t_{k-1}}^{t_k-1} \sigma_n^2(t)} \right).$$

In addition, letting

$$\theta_k = \frac{1}{t_k - t_{k-1}} \left[\sum_{t=t_{k-1}}^{t_k-1} (a_1(t) - \bar{a}_1(k))^2 + \sum_{t=t_{k-1}}^{t_k-1} (b_1(t) - \bar{b}_1(k))^2 + \sum_{t=t_{k-1}}^{t_k-1} \sigma_n^2(t) \right],$$

$$\alpha_k = \frac{1}{t_k - t_{k-1}} \sum_{t=t_{k-1}}^{t_k-1} (\bar{b}_1(k))^2, p_k = \frac{(t_k - t_{k-1})}{T}$$

due to the condition, θ_k is independent of k , which is denoted by θ . Thus, we have

$$F_{Y \rightarrow X}^{(c,S)} = \log \left(\frac{\sum_{t=1}^m \alpha_k p_k + \sum_{k=1}^m \theta_k p_k}{\sum_{k=1}^m \theta_k p_k} \right) = \log \left(\frac{\sum_{t=1}^m \alpha_k p_k + \theta}{\theta} \right),$$

and

$$F_{Y \rightarrow X}^{(a,S)} = \sum_{k=1}^m p_k \log \left(\frac{\alpha_k + \theta_k}{\theta_k} \right) = \sum_{k=1}^m p_k \log \left(\frac{\alpha_k + \theta}{\theta} \right).$$

Thus, we can conclude $F_{Y \rightarrow X}^{(a,S)} \leq F_{Y \rightarrow X}^{(c,S)}$, owing to the Jensen's inequality. This

completes the proof.

From Theorem C1, if the TV-MVAR system is time-varying with the segments well known, which implies that at each time window, the system is static, we can conclude that the average Grange causality is smaller than the cumulative Granger causality.

On the other hand, if the condition in Theorem C1 is not satisfied, then it will not be surprising that $F_{Y \rightarrow X}^{(a,S)} > F_{Y \rightarrow X}^{(c,S)}$ holds. Here is a counter-example. A special situation is to solve the time-varying regression model (A1) as a static one, i.e., taking all time points as the change-point set, i.e., $S = \{1, \dots, T+1\}$. By a proper transformation, we can still let the variances of y and x equal to 1 for all time. Let $a_1(t) = 0$ for all t . But the variance of the noise may be time-varying. The defined Granger causalities become:

$$F_{Y \rightarrow X}^S = \log \left(\frac{\frac{1}{T} \sum_{t=1}^T \sigma_n^2(t) + \frac{1}{T} \sum_{t=1}^T [b_1(t)]^2}{\frac{1}{T} \sum_{t=1}^T \sigma_n^2(t)} \right), \hat{F}_{Y \rightarrow X}^S = \frac{1}{T} \sum_{t=1}^T \log \left(\frac{\sigma_n^2(t) + [b_1(t)]^2}{\sigma_n^2(t)} \right).$$

Pick $T = 3, b_1 = 1, b_2 = \sqrt{2}, b_3 = \sqrt{3}, \sigma_1 = \sqrt{3}, \sigma_2 = \sqrt{2}, \sigma_3 = 1$. Then,

$$F_{Y \rightarrow X} = \log 2 < \hat{F}_{Y \rightarrow X} = \frac{1}{3} \left[\log \left(\frac{4}{3} \right) + \log(2) + \log(4) \right].$$

Comparison between the asymptotic square moments under null hypothesis.

For simplicity, we suppose that the time-varying system (A1) is a switching system with equal-length time windows and the segment points are exactly known. The general case will be treated in our future paper. Thus, (A1) becomes a series of static linear system as follows:

$$x^{t+1} = \bar{a}_1(k) x^t + \bar{b}_1(k) y^t + n(t), t_k \leq t < t_{k+1}, k = 1, 2, \dots, m, \quad (C1)$$

Here, $t_{k+1} - t_k = \frac{n}{m}$ for all k . Under the null hypothesis, namely, the coefficients $b_1(t) = 0$ hold for all t , (C1) becomes

$$x^{t+1} = \bar{a}_1(k) x^t + \tilde{n}(t), t_k \leq t < t_{k+1}, k = 1, 2, \dots, m. \quad (C2)$$

Their residual squared errors at each time window are

$$RSS_1(k) = \sum_{t=t_k}^{t_{k+1}-1} n^2(t) \quad \text{and} \quad RSS_0(k) = \sum_{t=t_k}^{t_{k+1}-1} \tilde{n}^2(t).$$

Then, the CGS and AGC can be formulated as follows respectively:

$$F_{Y \rightarrow X}^c = \log \left(\frac{\sum_{k=1}^m RSS_0(k)}{\sum_{k=1}^m RSS_1(k)} \right) = \log \left(1 + \frac{\sum_{k=1}^m [RSS_0(k) - RSS_1(k)]}{\sum_{k=1}^m RSS_1(k)} \right) \sim \frac{\sum_{k=1}^m [RSS_0(k) - RSS_1(k)]}{\sum_{k=1}^m RSS_1(k)}$$

$$F_{Y \rightarrow X}^a = \frac{1}{m} \sum_{k=1}^m \log \left(\frac{RSS_0(k)}{RSS_1(k)} \right) = \frac{1}{m} \sum_{k=1}^m \log \left(1 + \frac{RSS_0(k) - RSS_1(k)}{RSS_1(k)} \right) \sim \frac{1}{m} \sum_{k=1}^m \frac{RSS_0(k) - RSS_1(k)}{RSS_1(k)}$$

as n goes to infinity. Therefore, the cumulative Granger causality converges the following in distribution:

$$F_{Y \rightarrow X}^c \times \frac{n-2m-1}{m} \approx \frac{\sum_{k=1}^m [RSS_0(k) - RSS_1(k)]}{\sum_{k=1}^m RSS_1(k)} \times \frac{n-2m-1}{m} \sim F(m, n-2m-1)$$

and the average Granger causality converges to:

$$F_{Y \rightarrow X}^a \times \frac{n/m-3}{1} \approx \frac{1}{m} \sum_{k=1}^m \frac{RSS_0(k) - RSS_1(k)}{RSS_1(k)} \times \frac{n/m-3}{1}$$

with each

$$\frac{RSS_0(k) - RSS_1(k)}{RSS_1(k)} \times \frac{n/m-3}{1} \sim F(1, \frac{n}{m}-3)$$

So, their asymptotic expectations are

$$E(F_{Y \rightarrow X}^c) \approx \frac{m}{n-2m-1} \frac{n-2m-1}{n-2m-3} = \frac{1}{\frac{n}{m}-2-\frac{3}{m}}, \quad E(F_{Y \rightarrow X}^a) \approx \frac{\frac{n}{m}-3}{\frac{n}{m}-5} \frac{1}{\frac{n}{m}-3} = \frac{1}{\frac{n}{m}-5},$$

as $n \rightarrow \infty$.

The dominant converge rates are same, equivalently $\frac{m}{n}$. Then, let us take a look at their asymptotic square moments. By the square moment of the F -distribution and simple algebras, we have

$$E\left\{ [F_{Y \rightarrow X}^c]^2 \right\} \approx \left(1 + \frac{2}{m} \right) \left(\frac{m}{n} \right)^2.$$

As for the AGC, with $f_k = \frac{RSS_0(k) - RSS_1(k)}{RSS_1(k)} \sim F(1, \frac{n}{m}-3)$, we have

$$E\left\{\left[F_{Y \rightarrow X}^a\right]^2\right\} \cong \left(\frac{1}{n/m-3}\right)^2 E\left\{\frac{1}{m} \sum_{k=1}^m f_k\right\}^2 \leq \left(\frac{1}{n/m-3}\right)^2 \left(\frac{1}{m}\right) \sum_{k=1}^m E\{f_k\}^2$$

With

$$E\{f_k^2\} \cong 3 \left(\frac{\frac{n}{m}-3}{\frac{n}{m}-5}\right)^2,$$

which implies

$$E\left\{\left[F_{Y \rightarrow X}^a\right]^2\right\} < \frac{3}{m} \left(\frac{m}{n}\right)^2$$

holds in the asymptotic sense, i.e, if n is a sufficiently large. Therefore, in the asymptotic squared meaning, for $m > 1$, we have

$$E\left\{\left[F_{Y \rightarrow X}^a\right]^2\right\} < E\left\{\left[F_{Y \rightarrow X}^c\right]^2\right\}$$

asymptotically. In other words, the average Granger causality converges to zero more quickly than the cumulative Granger causality.

Theorem C2. Under the setup as mentioned above, $\limsup_{n \rightarrow \infty} \frac{E\left\{\left[F_{Y \rightarrow X}^a\right]^2\right\}}{E\left\{\left[F_{Y \rightarrow X}^c\right]^2\right\}} < 1$ for

$m > 1$.

And, the larger m is, the higher asymptotic converge rate the average Granger causality is than the cumulative one. □

Appendix D: Dual Kalman filter cumulative Granger causality (Dkf cumulative GC)

We used the dual Kalman filter as in (Havlicek et al., 2010; Sommerlade et al., 2012), which can be described as the following MVAR

$$\begin{bmatrix} x^{t+1} \\ y^{t+1} \end{bmatrix} = \sum_{k=1}^p A_k(t) \begin{bmatrix} x^{t-k} \\ y^{t-k} \end{bmatrix} + \begin{bmatrix} n_1^t \\ n_2^t \end{bmatrix} \quad (D1)$$

where $A_k(t)$ are the time-varying coefficients and $n_{1,2}^t$ are the white noises. Define

$$z^t = \begin{bmatrix} x^t \\ y^t \end{bmatrix}, \quad w(t) = \left[(z^t)^T, \dots, (z^{t-p+1})^T \right]^T, \quad a(t) = \text{vec} \left(\left[A_1(t)^T, \dots, A_p(t)^T \right] \right),$$

and Eq. (D1) can be rewritten as

$$z^t = w(t-1)^T a(t) + \eta^t \quad (D2)$$

associated with a random walk process for the time-varying coefficients

$$a(t+1) = a(t) + \nu^t. \quad (D3)$$

By the dual Kalman filter approach, the time-varying coefficients can be estimated, and then the residuals of Eq. (D2) can be used to define a cumulative GC by the same fashion as the cumulative GC in the paper

$$dkfGC_{Y \rightarrow X} = \log \left(\frac{\sum_{t=1}^T \text{var}(\eta_{yx}^t)}{\sum_{t=1}^T \text{var}(\eta_x^t)} \right), \quad (D4)$$

where T is the length of the time course, η_{yx}^t is the noise term in Eq. (D2) for the x -component *with considering the inter-dependence from y -component*, and η_x^t is the noise term in Eq. (D2) *without considering the inter-dependence from y -component*. As in (Havlicek et al., 2010), the $dkfGC_{Y \rightarrow X}$ and the $dkfGC_{X \rightarrow Y}$ can be computed by estimating the model parameters, and the p -value of these causality statistics can be established by bootstrap. The readers are refer to (Havlicek et al., 2010) for more details about the parameter estimation procedure and the bootstrap for significance.

References

- Ahmed, A., Xing, E., 2009. Recovering time-varying networks of dependencies in social and biological studies. *Proceedings of the National Academy of Sciences* 106, 11878-11883.
- Arichi, T., Fagiolo, G., Varela, M., Melendez-Calderon, A., Allievi, A., Merchant, N., Tusor, N., Counsell, S.J., Burdet, E., Beckmann, C.F., Edwards, A.D., 2012. Development of BOLD signal hemodynamic responses in the human brain. *NeuroImage* 63, 663-673.
- Biswal, B., Mennes, M., Zuo, X.-N., et.al., 2010. Toward discovery science of human brain function. *Proceedings of the National Academy of Sciences* 107, 4734-4739.
- Boyacioglu, R., Barth, M., 2012. Generalized iNverse imaging (GIN): Ultrafast fMRI with physiological noise correction. *Magn Reson Med* Up coming.
- Cavanna, A.E., Trimble, M.R., 2006. The precuneus: a review of its functional anatomy and behavioural correlates. *Brain*. 129, 564-583. Epub 2006 Jan 2006.
- Chen, M.-p., Lee, C.-C., Hsu, Y.-C., 2011. The impact of American depositary receipts on the Japanese index: Do industry effect and size effect matter? *Economic Modelling* 28, 526-539.
- Cribben, I., Haraldsdottir, R., Atlas, L.Y., Wager, T.D., Lindquist, M.A., 2012. Dynamic connectivity regression: determining state-related changes in brain connectivity. *Neuroimage*. 61, 907-920.

- Deshpande, G., Sathian, K., Hu, X., 2010. Effect of hemodynamic variability on Granger causality analysis of fMRI. *NeuroImage* 52, 884-896.
- Ding, M., Bressler, S.L., Yang, W., Liang, H., 2000. Short-window spectral analysis of cortical event-related potentials by adaptive multivariate autoregressive modeling: data preprocessing, model validation, and variability assessment. *Biological Cybernetics* 83, 35-45.
- Evan, K., Snigdhanu, C., Auroop R., G., 2011. Exploring Granger causality between global average observed time series of carbon dioxide and temperature. *Theoretical and Applied Climatology* 104, 325-335.
- Feinberg, D.A., Moeller, S., Smith, S.M., Auerbach, E., Ramanna, S., Glasser, M.F., Miller, K.L., Ugurbil, K., Yacoub, E., 2010. Multiplexed Echo Planar Imaging for Sub-Second Whole Brain fMRI and Fast Diffusion Imaging. *PLoS ONE* 5, e15710.
- Feinberg, D.A., Yacoub, E., 2012. The rapid development of high speed, resolution and precision in fMRI. *NeuroImage* 62, 720-725.
- Friston, K.J., Jezzard, P., Turner, R., 1994. Analysis of functional MRI time-series. *Human brain mapping* 1, 153-171.
- Ge, T., Feng, J., Grabenhorst, F., Rolls, E., 2012. Componential Granger causality, and its application to identifying the source and mechanisms of the top-down biased activation that controls attention to affective vs sensory processing. *NeuroImage* 59, 1846-1858.
- Ge, T., Kendrick, K., Feng, J., 2009. A Novel Extended Granger Causal Model Approach Demonstrates Brain Hemispheric Differences during Face Recognition Learning. *PLoS Comput Biol* 5, e1000570.
- Granger, C.W.J., 1969. Investigating Causal Relations by Econometric Models and Cross-spectral Methods. *Econometrica* 37, 424-438.
- Guo, S., Wu, J., Ding, M., Feng, J., 2008. Uncovering Interactions in the Frequency Domain. *PLoS Comput Biol* 4, e1000087.
- Havlicek, M., Friston, K.J., Jan, J., Brazdil, M., Calhoun, V.D., 2011. Dynamic modeling of neuronal responses in fMRI using cubature Kalman filtering. *NeuroImage* 56, 2109-2128.
- Havlicek, M., Jan, J., Brazdil, M., Calhoun, V.D., 2010. Dynamic Granger causality based on Kalman filter for evaluation of functional network connectivity in fMRI data. *Neuroimage*. 53, 65-77.
- Hemmelmann, D., Ungureanu, M., Hesse, W., Wustenberg, T., Reichenbach, J.R., Witte, O.W., Witte, H., Leistriz, L., 2009. Modelling and analysis of time-variant directed interrelations between brain regions based on BOLD-signals. *Neuroimage*. 45, 722-737.
- Hesse, W., Moller, E., Arnold, M., Schack, B., 2003. The use of time-variant EEG Granger causality for inspecting directed interdependencies of neural assemblies. *Journal of Neuroscience Methods* 124, 27-44.
- Jaynes, E.T., 1985. Some random observations. *Synthese* 63, 115-138.
- Lloyd, S., 1989. Use of mutual information to decrease entropy: implications for the second law of thermodynamics. *Physical Review A* 39, 5378-5386.
- Luo, Q., Ge, T., Feng, J., 2011. Granger causality with signal-dependent noise. *NeuroImage* 57, 1422-1429.
- Luscombe, N.M., Madan Babu, M., Yu, H., Snyder, M., Teichmann, S.A., Gerstein, M., 2004. Genomic analysis of regulatory network dynamics reveals large topological changes. *Nature* 431, 308-312.
- Ohiorhenuan, I.E., Mechler, F., Purpura, K.P., Schmid, A.M., Hu, Q., Victor, J.D., 2010. Sparse coding and high-order correlations in fine-scale cortical networks. *Nature* 466, 617-621.
- Psaridakis, Z., Ravn, M.O., Sola, M., 2005. Markov switching causality and the money-output

relationship. *Journal of Applied Econometrics* 20, 665-683.

Sato, J.o.R., Junior, E.A., Takahashi, D.Y., de Maria Felix, M., Brammer, M.J., Morettin, P.A., 2006. A method to produce evolving functional connectivity maps during the course of an fMRI experiment using wavelet-based time-varying Granger causality. *Neuroimage* 31, 187-196.

Schippers, M., Renken, R., Keysers, C., 2011. The effect of intra- and inter-subject variability of hemodynamic responses on group level Granger causality analyses. *NeuroImage* 57, 22-36.

Smerieri, A., Rolls, E.T., Feng, J., 2010. Decision Time, Slow Inhibition, and Theta Rhythm. *The Journal of neuroscience* 30, 14173-14181.

Smith, S.M., Bandettini, P.A., Miller, K.L., Behrens, T.E., Friston, K.J., David, O., Liu, T., Woolrich, M.W., Nichols, T.E., 2012. The danger of systematic bias in group-level FMRI-lag-based causality estimation. *NeuroImage* 59, 1228-1229.

Smith, S.M., Miller, K.L., Salimi-khorshidi, G., Webster, M., Beckmann, C.F., Nichols, T.E., Ramsey, J.D., Woolrich, M.W., 2011. Network modelling methods for FMRI. *NeuroImage* 54, 875-891.

Sommerlade, L., Thiel, M., Platt, B., Plano, A., Riedel, G., Grebogi, C., Timmer, J., Schelter, B., 2012. Inference of Granger causal time-dependent influences in noisy multivariate time series. *J Neurosci Methods* 203, 173-185.

Tuncbag, N., Kar, G., Gursoy, A., Keskin, O., Nussinov, R., 2009. Towards inferring time dimensionality in protein-protein interaction networks by integrating structures: the p53 example. *Mol. BioSyst.* 5, 1770-1778.

Tzourio-Mazoyer, N., Landeau, B., Papathanassiou, D., Crivello, F., Etard, O., Delcroix, N., Mazoyer, B., Joliot, M., 2002. Automated anatomical labeling of activations in SPM using a macroscopic anatomical parcellation of the MNI MRI single-subject brain. *Neuroimage.* 15, 273-289.

Wang, J., Zhu, H., Fan, J., Giovanello, K., Lin, W., 2011. Adaptively and spatially estimating the hemodynamic response functions in fMRI. *Med Image Comput Comput Assist Interv* 14, 269-276.

Warne, A., 2000. Causality and Regime Inference in a Markov Switching VAR. Sveriges Riksbank (Central Bank of Sweden).

Wen, X., Yao, L., Liu, Y., Ding, M., 2012. Causal interactions in attention networks predict behavioral performance. *The Journal of neuroscience* 32, 1284-1292.

Wiener, N., 1956. The Theory of Prediction. In: BeckenBach, E. (Ed.), *Modern mathematics for the engineer*. McGraw-Hill, New York, pp. 165 - 190.

Yan, C., Zang, Y., 2010. DPARSF: a MATLAB toolbox for "pipeline" data analysis of resting-state fMRI. *Frontiers in Systems Neuroscience* 4.

Zalesky, A., Fornito, A., Harding, I.H., Cocchi, L., Yucel, M., Pantelis, C., Bullmore, E.T., 2010. Whole-brain anatomical networks: does the choice of nodes matter? *NeuroImage* 50, 970-983.

Zhu, J., Chen, Y., Leonardson, A.S., Wang, K., Lamb, J.R., Emilsson, V., Schadt, E.E., 2010. Characterizing Dynamic Changes in the Human Blood Transcriptional Network. *PLoS Comput Biol* 6, e1000671.

Tables and Figure Captions

Table 1. The 95% confidence intervals of the differences between the cumulative causality measurements established from time windows with different lengths.

direction	$X \rightarrow Y$	$Y \rightarrow X$
-----------	-------------------	-------------------

quantile	0.025 th	0.975 th	0.025 th	0.975 th
D_1^a	0.0078	0.0321	0.0053	0.0341
D_2^a	0.0085	0.0448	0.0109	0.0453
D_3^a	0.0002	0.0128	0.0003	0.0229
D_1^c	0.0078	0.0285	0.0055	0.0333
D_2^c	0.0105	0.0437	0.0116	0.0480
D_3^c	0.0002	0.0156	0.0003	0.0264

Table 2. Performance comparison for different methods. ‘Classical GC’ is short for the classic Granger causality. ‘Cumulative GC’ is the cumulative Granger causality. ‘Average GC’ is the average Granger causality. ‘opt Cumulative GC’ stands for the cumulative Granger causality with optimally divided time windows, and ‘opt Average GC’ means the average Granger causality with optimally determined time windows. $\bar{F}_{X \rightarrow Y}$ and $\bar{F}_{Y \rightarrow X}$ are the average values of the Granger causality measurements over 100 simulations, and \overline{BIC} is the mean value of the BIC for 100 simulations. The threshold for significance is 1e-11.

Method	Window Length	TP	FP	TN	FN	$\bar{F}_{X \rightarrow Y}$	$\bar{F}_{Y \rightarrow X}$	\overline{BIC}
Classical GC	1200	0%	0%	100%	100%	0.0023	0.0007	6.9489
Cumulative GC	10	50%	0%	100%	50%	0.2484	0.1331	8.5869
	50	72%	0%	100%	28%	0.1303	0.0208	7.2041
	100	75%	0%	100%	25%	0.1177	0.0101	7.0188
	300	70%	0%	100%	30%	0.0709	0.0032	6.9417
	600	0%	0%	100%	100%	0.0071	0.0015	6.9819
Average GC	10	39%	0%	100%	61%	0.2620	0.1516	8.5869
	50	85%	0%	100%	15%	0.1219	0.0212	7.2041

	100	93%	0%	100%	7%	0.1094	0.0102	7.0188
	300	92%	0%	100%	8%	0.0681	0.0032	6.9417
	600	14%	0%	100%	86%	0.0074	0.0015	6.9819
Opt Cumulative GC		90%	3%	97%	10%	0.1320	0.0131	6.8780
Opt Average GC		94%	2%	98%	6%	0.1453	0.0080	6.8780

Table 3. Comparison of running time (in second) for different methods. The classic Granger causality treated the whole time series as one time window. The average Granger causality and the cumulative Granger causality were applied to the data by dividing the time series into time windows with equal lengths. The average Granger causality and the cumulative Granger causality had also been used after optimally dividing the time windows by the proposed algorithm. This simulation was carried out by a computer with Intel® Core™ 2 CPU T5600 @ 1.83GHz, 1.83GHz, and 1.5G RAM.

	One time window	Time windows with equal length					Optimally divided time windows
Window length	1200	600	300	100	50	10	
Running time	0.0073	0.2936	0.4697	0.9969	1.9747	9.8709	346.5863

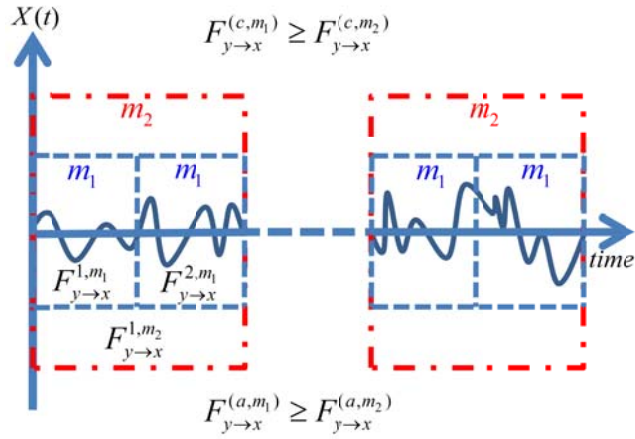


Figure 1. Monotonicity of the cumulative Granger causality and the average Granger causality respectively. If we consider finer time windows with the same length, the change-point set can be derived from the window length, so the causality established by different change-point sets can be equivalently denoted by the corresponding window lengths m_i for S_i .

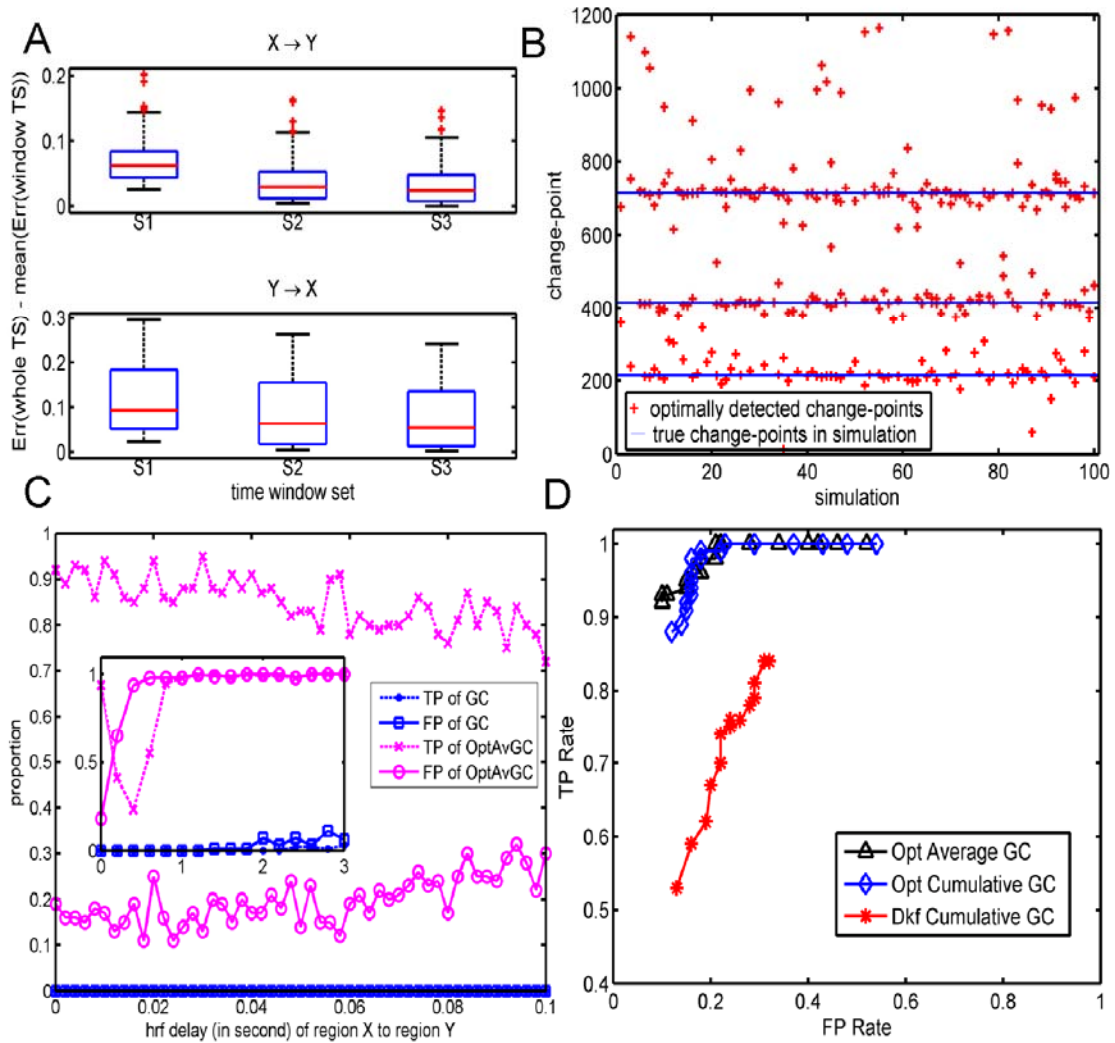


Figure 2. Results for simulation model: (A) Residual variance comparison between the models established from the whole time series and those models fitted on different time window sets. (B) Optimally detected change-points for 100 simulations. (C) Mean of TP rate and FP rate given by different methods for each HRF delay in 100 simulations. (D) The TP rate is plotted against the FP rate given by different approaches for each threshold of p-values in 100 simulations

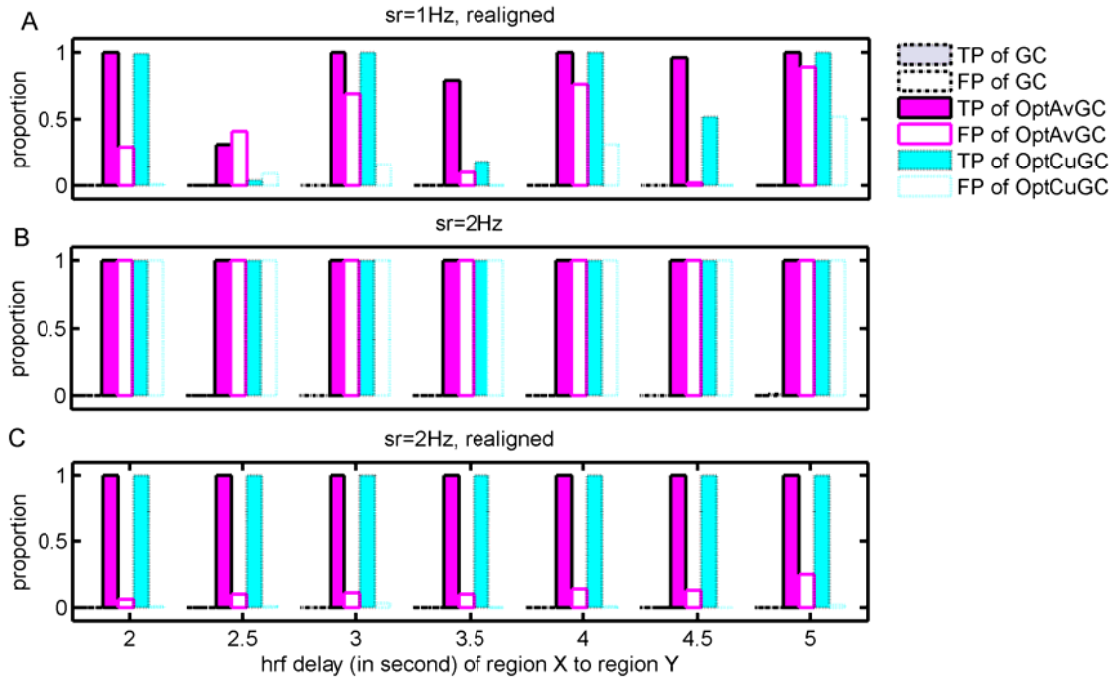


Figure 3. Effects of HRF delay and down sampling on the Granger causality analysis (GCA). **A)** Performances of GCA's after the realignment of the BOLD signals between two regions to correct the opposite HRF delay when the sampling rate was 1Hz; **B)** Performances of GCA's when the sampling rate was 2Hz; **C)** Performances of GCA's after the realignment of the BOLD signals when the sampling rate was 2Hz.

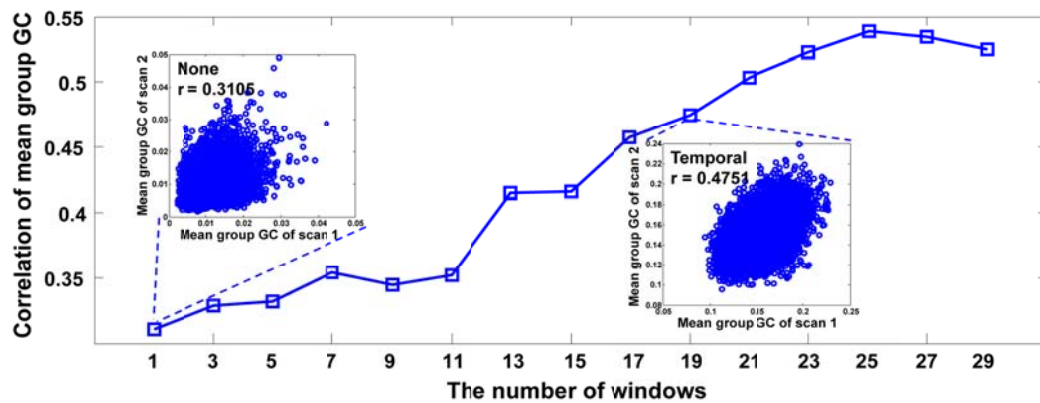


Figure 4. Correlation of the mean group Granger causalities (GC) between two series of scanning upon the same subject set versus the number of time windows for the average Granger causality. The inset plots show the correlation between two scans of selected the number of windows, in which each circle represents the GC between two ROIs parcelled by AAL atlas.

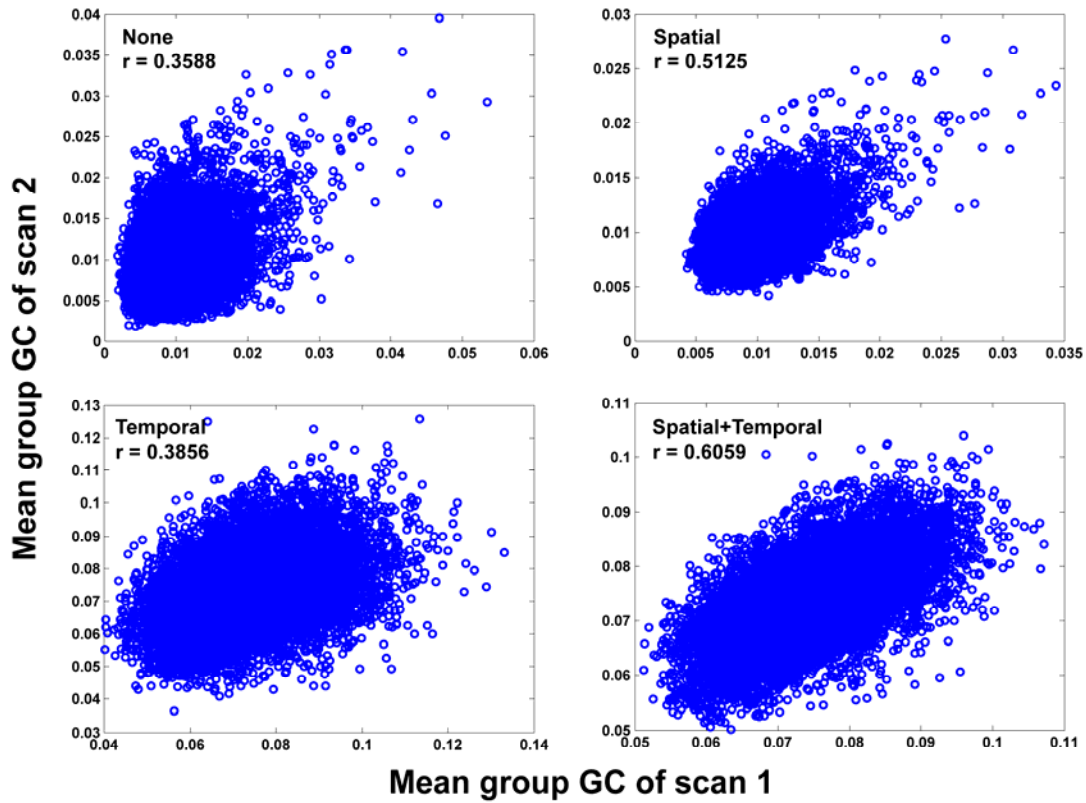


Figure 5. Correlation between the Granger causality between two series of scanning upon the same subject set. The causality measurements were calculated by different methods: (A) the traditional Granger causality; (B) the voxel level Granger causality; (C) the average Granger causality; (D) the spatial-temporal Granger causality.

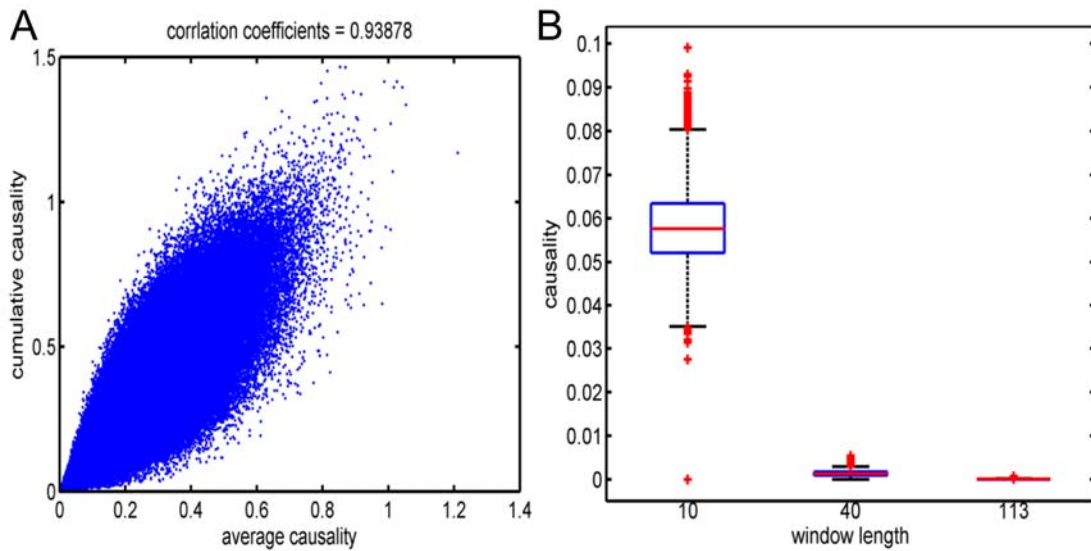


Figure 6. Granger causality results of the resting-state data set. (A) Average Granger causality versus cumulative Granger causality on the resting state data set. (B)

Comparison of the average Granger causality established by different time window lengths.

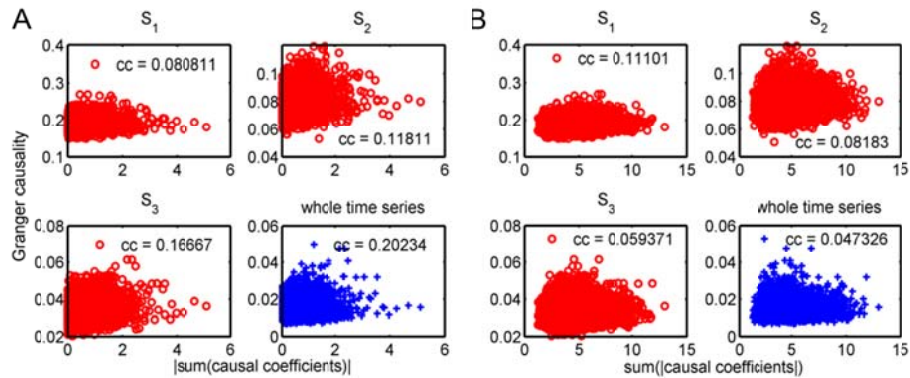


Figure 7. Granger causality versus the sum of the causal coefficients across time windows. The causal coefficients were estimated for each time window defined by S_1 for each subject. The medians of the causality among 198 subjects were established by different change-point sets, including S_1, S_2, S_3 and the whole time series without change-point (specified as the titles for subplots in the figure). Different change-point sets gave different Granger causality value, since the Granger causality value increased as the time window lengths decrease. (A) Correlation to the absolute value of the median of the sum of the causal coefficients over all time windows; (B) Correlation to the median of the sum of the absolute value of the causal coefficients over all time windows. The p -values for all correlations are below the significant threshold.

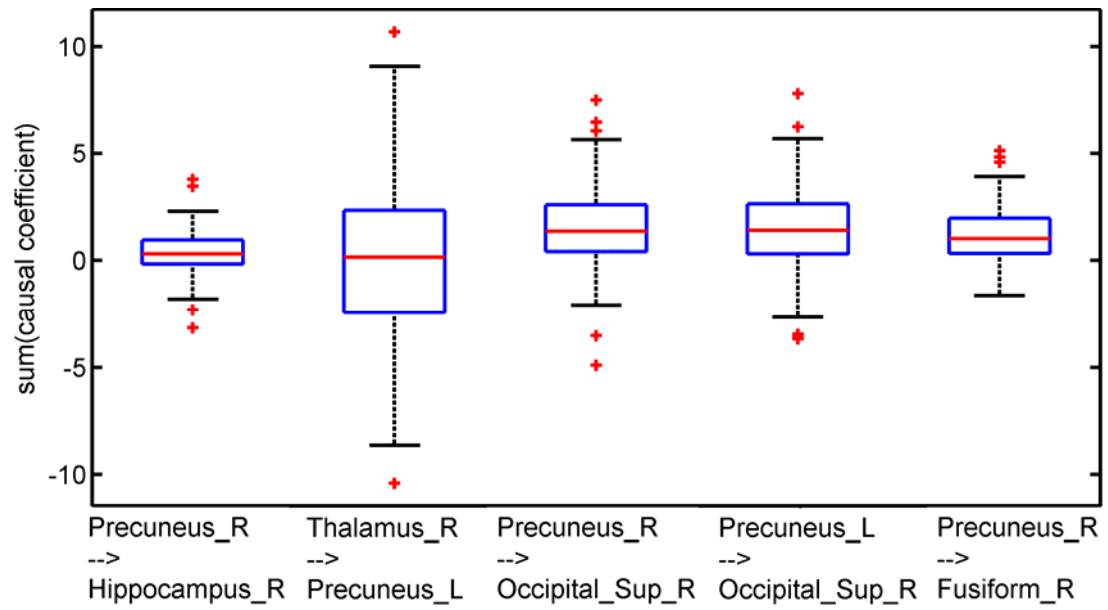


Figure 8. Boxplot for sum of the causal coefficients across all time windows of the change-point set \mathcal{S}_1 .

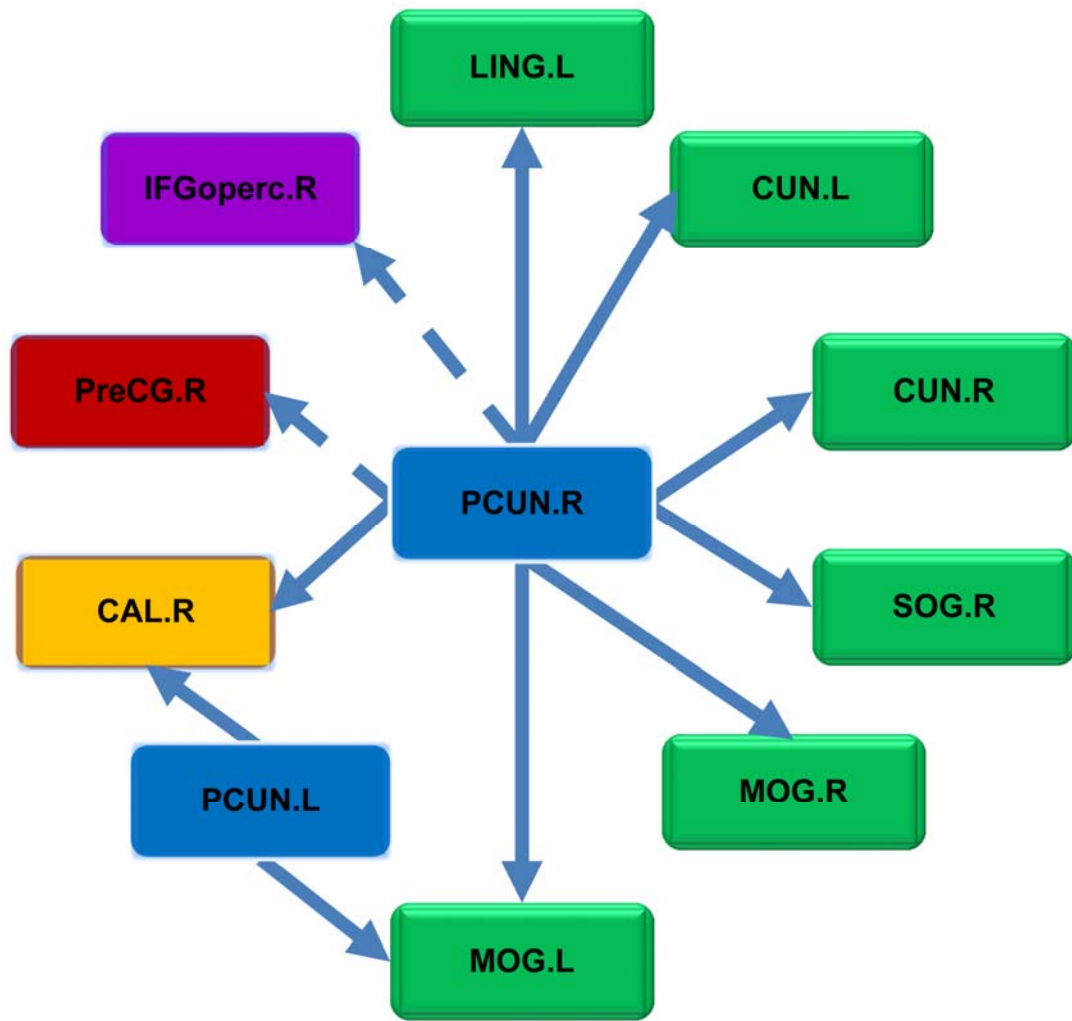


Figure 9.Information flows from precuneus inferred by the average Granger causality based on the optimal time window dividing algorithm. Brain regions for visual recognition are marked in green, primary visual cortex marked in yellow, sensory motor areas marked in red, attention areas in purple. Those arrows marked by dot lines may be false predictions due to the regional variation of HRF. The brain regions are defined by AAL90 as in DPARSF(Yan and Zang, 2010).

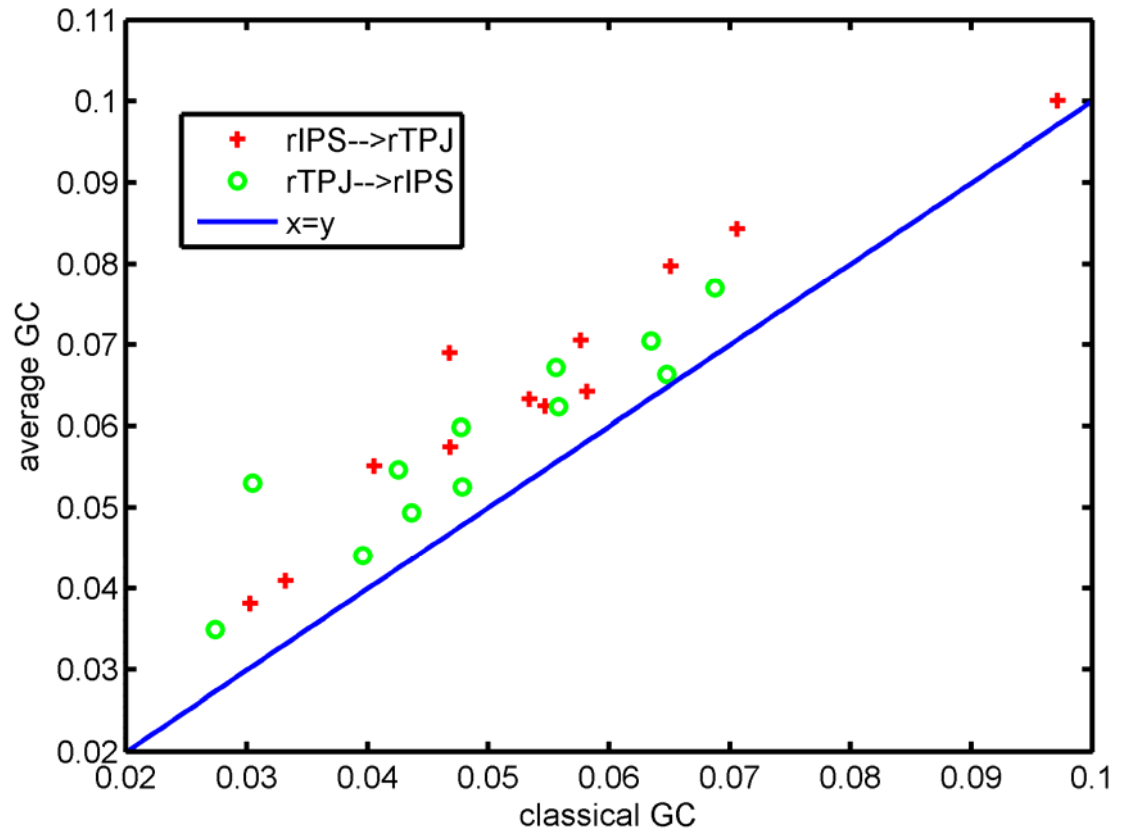


Figure 10. Comparison between the classic Granger causality (classical GC) and the average Granger causality (average GC) for the attention-task dataset.